Localized Artificial Viscosity Stabilization of Discontinuous Galerkin Methods for Nonhydrostatic Mesoscale Atmospheric Modeling

M. L. YU

University of Maryland, Baltimore County, Baltimore, Maryland

F. X. GIRALDO

Naval Postgraduate School, Monterey, California

M. PENG

U. S. Naval Research Laboratory, Monterey, California

Z. J. WANG

University of Kansas, Lawrence, Kansas

(Manuscript received 13 March 2015, in final form 31 August 2015)

ABSTRACT

Gibbs oscillation can show up near flow regions with strong temperature gradients in the numerical simulation of nonhydrostatic mesoscale atmospheric flows when using the high-order discontinuous Galerkin (DG) method. The authors propose to incorporate flow-feature-based localized Laplacian artificial viscosity in the DG framework to suppress the spurious oscillation in the vicinity of sharp thermal fronts but not to contaminate the smooth flow features elsewhere. The parameters in the localized Laplacian artificial viscosity are modeled based on both physical criteria and numerical features of the DG discretization. The resulting numerical formulation is first validated on several shock-involved test cases, including a shock discontinuity problem with the one-dimensional Burger's equation, shock–entropy wave interaction, and shock–vortex interaction. Then the efficacy of the developed numerical formulation on stabilizing thermal fronts in nonhydrostatic mesoscale atmospheric modeling is demonstrated by two benchmark test cases: the rising thermal bubble problem and the density current problem. The results indicate that the proposed flow-feature-based localized Laplacian artificial viscosity method can sharply detect the nonsmooth flow features, and stabilize the DG discretization nearby. Furthermore, the numerical stabilization method works robustly for a wide range of grid sizes and polynomial orders without parameter tuning in the localized Laplacian artificial viscosity.

1. Introduction

Numerical weather prediction (NWP) models have been profoundly influenced by the paradigm shift in high performance computing (HPC). On the one hand, the ever increasing computing power allows researchers to run nonhydrostatic (NH) models at resolutions finer than 10 km (Steppeler et al. 2003; Lynch 2008; Marras et al. 2015); on the other, both HPC and the intrinsic complex physical processes in NH modeling pose many challenges to the development of numerical methods (e.g., local numerical algorithms, high-order accuracy, geometric flexibility, etc.). The discontinuous Galerkin (DG) method has been proven to be an ideal candidate to accommodate these challenges (Giraldo and Restelli 2008). One example is the Nonhydrostatic Unified Model of the Atmosphere (NUMA) (Kelly and Giraldo 2012; Giraldo et al. 2013), which has been successfully applied to three-dimensional limited-area modeling on distributed-memory computers with a large number of processors as well as with adaptive mesh refinement (AMR) in two dimensions (Kopera and Giraldo 2014).

Despite the success in NH modeling by high-order accurate (i.e., order > 2) methods (Giraldo and Restelli

Corresponding author address: Meilin Yu, University of Maryland, Baltimore County, 1000 Hilltop Circle, Baltimore, MD 21250. E-mail: mlyu@umbc.edu

DOI: 10.1175/MWR-D-15-0134.1

2008; Ullrich and Jablonowski 2012), robust and efficient stabilization of sharp flow gradients (e.g., thermal fronts) or flow discontinuities (e.g., shock) remains challenging in the design of high-order methods. Arguably, the two most frequently adopted methods to stabilize the high-order methods in the presence of nonsmooth flow features are limiters; for example, the total variation bounded (TVB) limiter, the positivity preserving limiter, the weighted essentially nonoscillatory (WENO) limiter in the numerical framework of Runge–Kutta discontinuous Galerkin (RKDG) (Cockburn and Shu 1998; Qiu and Shu 2005; Zhang and Shu 2010; Zhang and Nair 2012), and artificial viscosity. In the limiter approach, the distribution of flow variables is reshaped explicitly via the limiting procedure, whereas in the artificial viscosity approach, no direct modification is applied to the flow variables. Instead, an artificial diffusion process is designed to smooth out oscillation due to flow discontinuities or sharp fronts. Both limiters and artificial viscosity have been successfully applied in shock capturing for supersonic and hypersonic flows using discontinuous high-order methods (Cockburn and Shu 1998; Qiu and Shu 2005; Zhang and Shu 2010; Persson and Peraire 2006; Yang and Wang 2009; Dedner and Klöfkorn 2011; Yu and Wang 2014; Park et al. 2014).

In the numerical simulation of nonhydrostatic mesoscale atmospheric modeling, very high-order polynomials can be used to approximate the solution, as shown by Giraldo and Restelli (2008). Under this scenario, the implementation of hierarchical limiters will be very complicated. Furthermore, after limiting, the solution might be represented by a lower-order or even piecewise constant reconstruction. This polynomial order reduction will dramatically increase the numerical dissipation of the DG algorithm in the neighborhood of the limited element. Sometimes, key flow features can be totally smeared out, especially on coarse meshes. Artificial viscosity provides an alternative way to handle very high-order simulations on coarse (i.e., underresolved) meshes in the presence of sharp fronts.

The idea of capturing shock wave discontinuities in a fluid by adding artificial viscosity into hyperbolic conservation laws originated from Von Neumann and Richtmyer (1950). Since then, many types of artificial viscosity methods have been developed to deal with flow discontinuity capturing. One crucial issue in all artificial viscosity modeling is how to describe the smoothness of the flow fields accurately. Smoothness indicators are used for this purpose. Different smoothness indicators have been designed based on the gradient of flow quantities (e.g., velocity, internal energy, etc.) (Cook and Cabot 2004; Kawai and Lele 2008), resolution of the numerical representation (Tadmor 1990; Persson and Peraire 2006), residual/entropy residual of the simulation (Bassi and Rebay 1994; Hartmann and Houston 2002; Guermond and Pasquetti 2008), and so on. Note that all these smoothness indicators can effectively localize the artificial viscosity in the vicinity of flow discontinuities. Based on the different procedures to design artificial diffusive terms and to incorporate them into the original governing equations, the artificial viscosity methods for computational fluid dynamics can be roughly classified into several categories. These include, but are not limited to the streamline-upwind/Petrov–Galerkin (SUPG)-type artificial viscosity (Hughes and Mallet 1986; Tezduyar and Park 1986; Johnson et al. 1990; Tezduyar and Senga 2006), variational multiscale (VMS) (Marras et al. 2012, 2013), localized artificial diffusivity using physical principles (Cook and Cabot 2004; Kawai and Lele 2008; Cook 2007; Kawai et al. 2010; Premasuthan et al. 2010; Olson and Lele 2013; Haga and Kawai 2013), residual-based artificial viscosity (Bassi and Rebay 1994; Hartmann and Houston 2002; Bassi et al. 1997; Hartmann 2006; Kurganov and Liu 2012), entropy artificial viscosity (Guermond and Pasquetti 2008; Guermond et al. 2011; Zingan et al. 2013), spectral vanishing viscosity (Tadmor 1990; Oberai and Wanderer 2006), and Laplacian or higher-order artificial viscosity (Persson and Peraire 2006; Wicker and Skamarock 1998; Xue 2000; Barter and Darmofal 2010; Klöckner et al. 2011; Persson 2013; Li et al. 2013; Yelash et al. 2014) methods. Other studies of the artificial viscosity methods can be found in the studies by Jameson (1995), Caramana et al. (1998), Huang et al. (2005), Klemp et al. (2007), Skamarock and Klemp (2008), Jebens et al. (2009), Kolev and Rieben (2009), Nair (2009), and Reisner et al. (2013), just to name a few.

We note that in many numerical simulations for nonhydrostatic mesoscale atmospheric modeling, a small amount of constant numerical viscosity is added to the entire flow field to smooth out noises generated due to insufficient resolution of small-scale flow features, functioning similarly as a filter. This approach has been demonstrated successfully to suppress numerical instability due to high-frequency aliasing errors. However, artificial viscosity added to the entire flow field will dissipate the solution near smooth flow features, and cannot automatically adapt with numerical discretization (i.e., when the grid resolution is altered). For the atmospheric flow over topography, when constant viscosity or hyperviscosity is used, mass and potential temperature can be diffused along terrain-following surfaces leading to loss of hydrostatic balance and generation of spurious vertical noise. To overcome the

aforementioned deficits of constant viscosity or hyperviscosity, some previous studies (e.g., Boyd 1996; Schär et al. 2002; Guba et al. 2014) have been carried out. The basic concepts from those studies are to incorporate scale-dependent numerical dissipation, which can be based on the flow features, terrain features, or computational grid features. In the work by Boyd (1996), a continuously varying Erfc-Log filter is designed based on the distance between the current location and the singularity. As a result, it can smooth out oscillation near the discontinuity while maintaining the smooth region almost unaffected. Schär et al. (2002) developed a new terrain-following vertical coordinate formulation that can suppress small-scale noises due to grid inhomogeneity by employing a scale-dependent vertical decay of underlying terrain features. Guba et al. (2014) developed a tensor-based hyperviscosity for variable-resolution grids. Using the shallow-water equations in spherical geometry, it is demonstrated that no grid-dependent oscillation shows up in the transition region of grids with different resolution.

In this study, a flow-feature-based artificial viscosity is proposed to smear high-frequency oscillations near sharp flow features, while not affecting the smooth flow fields elsewhere. Considering the features of the governing equations (Giraldo and Restelli 2008), we augment the original hyperbolic system with the flow-feature-based localized Laplacian artificial diffusive terms (Persson and Peraire 2006). The proposed localized Laplacian artificial viscosity is constructed based on the smoothness of the flow fields. Therefore, an adequate amount of artificial viscosity is localized in the vicinity of sharp fronts to suppress the Gibbs oscillation. Meanwhile, vanishing artificial viscosity does not contaminate the smooth flow features away from sharp fronts.

The remainder of the paper is organized as follows. The governing equations for the nonhydrostatic mesoscale atmospheric modeling and the discontinuous Galerkin discretization are introduced in section 2. In section 3, the basic ideas behind the localized Laplacian artificial viscosity method are reviewed. A new family of modified localized Laplacian artificial viscosity models is introduced based on the proposed modeling principles. Section 4 then presents the numerical results from simulations of benchmark test cases. The sensitivity of free parameters in artificial viscosity modeling is also studied there. Finally, conclusions are summarized in section 5.

2. Governing equations and discretization

Many different forms of the governing equations have been used for numerical weather prediction together with various numerical methods. For nonhydrostatic atmospheric modeling, three sets of equations were presented by Giraldo and Restelli (2008): the nonconservative form using Exner pressure, momentum, and potential temperature (set 1); the conservative form using density, momentum, and potential temperature (set 2); and the conservative form using density, momentum, and total energy (set 3). Note that in the nonconservative form (set 1), the mass equation is defined by a conservation-like law for the Exner pressure, which cannot be formally conserved. As a result, the model based on these governing equations cannot conserve either mass or energy. In contrast, both mass and energy are conserved in the conservative form (sets 2 and 3). It was found by Giraldo and Restelli (2008) that the two conservative forms outperform the nonconservative form. Therefore, we study equation set 2 in this paper, which is one of the equation sets used in the NUMA model (Kelly and Giraldo 2012; Giraldo et al. 2013) and is a good compromise between conservation and efficiency.

a. Governing equations

The two-dimensional form of equation set 2 reads as

$$\frac{\partial Q}{\partial t} + \nabla \cdot \mathbf{F}(Q) = G(Q), \tag{1}$$

where $Q = (\rho, \rho u, \rho w, \rho\theta)$ are the conservative variables; ρ is the density; u and w are velocities in x and z directions, respectively; θ is the potential temperature; $\mathbf{F} = (f^x, f^z)$ is the inviscid flux; and G is the source term. They are defined as

$$f^x = \begin{pmatrix} \rho u \\ \rho u^2 + p \\ \rho uw \\ \rho u\theta \end{pmatrix}, \quad f^z = \begin{pmatrix} \rho w \\ \rho uw \\ \rho w^2 + p \\ \rho w\theta \end{pmatrix}, \quad \text{and}$$

$$G = \begin{pmatrix} 0 \\ 0 \\ -\rho g \\ 0 \end{pmatrix}, \tag{2}$$

where g is the gravitational constant, p is the pressure, and is related with θ by the equation of state as follows:

$$p = p_0 \left(\frac{\rho R\theta}{p_0} \right)^{\gamma}, \tag{3}$$

where $\gamma = C_p/C_v$ is the ratio of specific heats (for constant pressure and constant volume), R is the gas constant, and p_0 is a reference pressure that is only a function of the vertical coordinate. Introducing the splitting of the density, pressure and potential temperature as $\rho = \rho_0 + \rho'$,

$p = p_0 + p'$, and $\theta = \theta_0 + \theta'$, where the subscript "0" denotes the values in hydrostatic balance, we rewrite Eq. (1) as

$$\frac{\partial Q'}{\partial t} + \nabla \cdot \mathbf{F}'(Q) = G'(Q), \tag{4}$$

where $Q' = (\rho', \rho u, \rho w, \Theta')$, $\Theta = \rho\theta$, and $\Theta' = \Theta - \rho_0\theta_0$. Correspondingly, $\mathbf{F}'$ is written as

$$f^{x'} = \begin{pmatrix} \rho u \\ \rho u^2 + p' \\ \rho uw \\ \rho u\theta \end{pmatrix}, \quad f^{z'} = \begin{pmatrix} \rho w \\ \rho uw \\ \rho w^2 + p' \\ \rho w\theta \end{pmatrix}, \quad \text{and}$$

$$G' = \begin{pmatrix} 0 \\ 0 \\ -\rho' g \\ 0 \end{pmatrix}. \tag{5}$$

The governing equations are solved on the physical domain Ω, which is partitioned into N nonoverlapping elements Ω^i. The solution Q_i' on each element Ω^i belongs to $\mathbb{Q}^k(\Omega^i)$, where $\mathbb{Q}^k(\Omega^i)$ is the space of tensor product of polynomials of degree at most k in each variable defined on Ω^i. For conciseness, the element-wise continuous solution Q_i' is replaced with Q_i in the following sections when no confusion between Q_i' and Q_i exists. The same convention also applies to $\mathbf{F}'$ and G'.

b. Discontinuous Galerkin method

We approximate the exact solution of the conservation law using an element-wise continuous polynomial $Q_h \in V_h^{\mathrm{DG}} = \{W \in L^2(\Omega^i)\}$. Herein, V_h^{DG} is a finite-element space for DG, and $L^2(\Omega^i)$ is the space of square integrable functions defined on Ω^i. Let W be an arbitrary weighting function or test function from the same space V_h^{DG}. The weighted residual form of the governing equations on each element Ω^i then reads

$$\int_{\Omega^i} \frac{\partial Q_h}{\partial t} W \, dV + \int_{\Omega^i} \nabla \cdot \mathbf{F}(Q_h) W \, dV = \int_{\Omega^i} G(Q_h) W \, dV, \quad \forall \quad W \in V_h^{\mathrm{DG}}. \tag{6}$$

Applying integration by parts to Eq. (6), one obtains

$$\int_{\Omega^i} \frac{\partial Q_h}{\partial t} W \, dV - \int_{\Omega^i} \nabla W \cdot \mathbf{F}(Q_h) \, dV + \int_{\partial\Omega^i} \mathbf{F} \cdot \mathbf{n} W \, dS = \int_{\Omega^i} G(Q_h) W \, dV, \tag{7}$$

where $\mathbf{F} = (f^x, f^z)$ and $\mathbf{n}$ is the outward unit normal vector of $\partial\Omega^i$.

It is clear that the surface integral in Eq. (7) is not properly defined as the numerical solution is discontinuous across element interfaces. To ensure conservation, the normal flux term $\mathbf{F} \cdot \mathbf{n}$ is replaced with a Riemann flux $F^n_{\mathrm{com}}(Q_h^i, Q_h^{i+}, \mathbf{n})$, where Q_h^{i+} denotes the solution outside the current element Ω^i. Various (approximate) Riemann solvers can be used to calculate the Riemann flux, and the Rusanov Riemann solver is adopted in this paper. Then Eq. (7) can be rewritten as

$$\int_{\Omega^i} \frac{\partial Q_h}{\partial t} W \, dV - \int_{\Omega^i} \nabla W \cdot \mathbf{F}(Q_h) \, dV + \int_{\partial\Omega^i} F^n_{\mathrm{com}}(Q_h^i, Q_h^{i+}, \mathbf{n}) W \, dS = \int_{\Omega^i} G(Q_h) W \, dV. \tag{8}$$

In the DG approach, a finite-dimensional basis set $\{W_j\}$ is chosen as the solution space. Then the governing equation is projected onto each member of the basis set [see also the work by Hesthaven and Warburton (2008)]. Thus, Eq. (8) is reformulated as

$$\frac{\partial}{\partial t} \int_{\Omega^i} W_k \sum_j (Q_{h,j} W_j) \, dV - \int_{\Omega^i} \nabla W_k \cdot \mathbf{F}(Q_h) \, dV + \int_{\partial\Omega^i} W_k F^n_{\mathrm{com}} \, dS = \int_{\Omega^i} W_k \sum_j (G_j W_j) \, dV. \tag{9}$$

Applying integration by parts again to the second term of Eq. (9), the strong form of DG is obtained as

$$\frac{\partial}{\partial t} \int_{\Omega^i} W_k \sum_j (Q_{h,j} W_j) \, dV + \int_{\Omega^i} W_k \nabla \cdot \mathbf{F}(Q_h) \, dV + \int_{\partial\Omega^i} W_k (F^n_{\mathrm{com}} - F^n) \, dS = \int_{\Omega^i} W_k \sum_j (G_j W_j) \, dV, \tag{10}$$

where $F^n = \mathbf{F} \cdot \mathbf{n}$ is the local flux projected on $\partial\Omega^i$ in the surface normal direction.

The first integral in Eq. (10) is usually written as a multiplication of the mass matrix $\mathbf{M}$ and the time derivative of the solution vector $[Q_h]$. The square bracket "[ ]" denotes the vector form of the solution Q_h. The entries of the mass matrix $\mathbf{M}$ are of the following form:

$$M_{(k,j)} = \int_{\Omega^i} W_k W_j \, dV. \tag{11}$$

If $\mathbf{F}$ is a linear function of Q, then $\mathbf{F}$ can be expressed as $\mathbf{F} = \sum_j \mathbf{F}_j W_j$. Under this constraint, the second integral in Eq. (10) can be formulated as a multiplication of the stiffness matrix $\mathbf{S}^l$ and the flux vector $[F^l]$. The entries of the stiffness matrix $\mathbf{S}^l$ are written as

$$S^l_{(k,j)} = \int_{\Omega^i} W_k \frac{\partial W_j}{\partial x^l} dV, \quad l = 1, 2. \tag{12}$$

However, if $\mathbf{F}$ is a nonlinear function of Q, then $\mathbf{F}$ cannot generally be expressed via the basis set $\{W_j\}$. Quadratures are used to compute the volume and surface integrals. Clearly these operations can be expensive, and some cost-effective approaches are required to improve the computational efficiency. One such solution is the quadrature-free approach proposed by Atkins and Shu (1998). In this approach, it is assumed that even if the flux $\mathbf{F}$ is nonlinear, it still can be represented by a polynomial that belongs to the same space $\mathbb{Q}^k(\Omega^i)$ as that of the solution Q_h. We denote it by $\mathbf{F}_h$. Then Eq. (10) still holds for $\mathbf{F}_h$.

We also assume that F^n_{com} belongs to the polynomial space $P^k(\partial\Omega^i)$ and can be expressed by the basis set $\{W_{f,j}\}$ as $F^n_{\text{com},f} = \sum_j F^n_{\text{com},f,j} W_{f,j}$ on each surface. Thus, the mass matrices $\mathbf{B}_f$ for the surface integration in Eq. (10) can be formed with the following entries:

$$B_{f,(k,j)} = \int_f W_k W_{f,j}\, dS_f. \tag{13}$$

Substituting Eqs. (11)–(13) into Eq. (10), we obtain the following vector form:

$$\frac{\partial [Q_h]}{\partial t} = -\sum_{l=1}^{2} (\mathbf{M}^{-1}\mathbf{S}^l)[F^l] - \sum_f (\mathbf{M}^{-1}\mathbf{B}_f)[F^n_{\text{com},f} - F^n_f] + [G_h]. \tag{14}$$

Now consider the nodal-type allocation of degrees of freedom (DOFs), and assume that W_m is the Lagrange polynomial, which satisfies $W_m(\mathbf{r}_j) = \delta_{mj}$, where $\mathbf{r}_j = (x_j, z_j)$ is the nodal point. Following the work by Hesthaven and Warburton (2008), we introduce the differentiation matrix $\mathbf{D}_{x^l}$, with the following entries:

$$D_{x^l,(j,m)} = \left.\frac{\partial W_m}{\partial x^l}\right|_{\mathbf{r}_j}. \tag{15}$$

Then the entries of $\mathbf{MD}_{x^l}$ can be calculated as

$$\begin{aligned}(\mathbf{MD}_{x^l})_{(k,m)} &= \sum_j \int_{\Omega^i} W_k W_j \left.\frac{\partial W_m}{\partial x^l}\right|_{\mathbf{r}_j} dV \\ &= \int_{\Omega^i} W_k \sum_j W_j \left.\frac{\partial W_m}{\partial x^l}\right|_{\mathbf{r}_j} dV \\ &= \int_{\Omega^i} W_k \frac{\partial W_m}{\partial x^l} dV = (\mathbf{S}^l)_{(k,m)}.\end{aligned} \tag{16}$$

Therefore, Eq. (14) can be rewritten as

$$\frac{\partial [Q_h]}{\partial t} = -\sum_{l=1}^{2} \mathbf{D}_{x^l}[F^l] - \sum_f (\mathbf{M}^{-1}\mathbf{B}_f)[F^n_{\text{com},f} - F^n_f] + [G_h]. \tag{17}$$

According to Eq. (17), in the implementation of the strong form, there is no need to explicitly calculate the stiffness matrix $\mathbf{S}^l$, but the differentiation of the flux polynomials. This fact can be utilized to save computational cost, as demonstrated by Yu et al. (2014). More detailed information about this implementation can be found in the work by Giraldo and Restelli (2008).

3. Localized Laplacian artificial viscosity

The localized Laplacian artificial viscosity is used to suppress the Gibbs oscillation near sharp thermal fronts. Generally, for two-dimensional problems, the Laplacian diffusion terms $\nabla \cdot \mathbf{F}^{\text{av}}(Q, \nabla Q)$ in x and z directions read as follows:

$$f^{\text{av}} = \begin{pmatrix} 0 \\ \varepsilon_{e,x}\rho \dfrac{\partial u}{\partial x} \\ \varepsilon_{e,x}\rho \dfrac{\partial w}{\partial x} \\ \varepsilon_{e,x}\rho \dfrac{\partial \theta'}{\partial x} \end{pmatrix} \quad \text{and} \quad g^{\text{av}} = \begin{pmatrix} 0 \\ \varepsilon_{e,z}\rho \dfrac{\partial u}{\partial z} \\ \varepsilon_{e,z}\rho \dfrac{\partial w}{\partial z} \\ \varepsilon_{e,z}\rho \dfrac{\partial \theta'}{\partial z} \end{pmatrix}. \tag{18}$$

For simplicity, we set $\varepsilon_{e,x} = \varepsilon_{e,z} = \varepsilon_e$.

The DG method is used to discretize the following equivalent system of Eq. (4) augmented by the artificial diffusion term $\nabla \cdot \mathbf{F}^{\text{av}}(Q, \nabla Q)$,

$$\begin{cases} \mathbf{R} - \nabla Q = 0, \\ \dfrac{\partial Q}{\partial t} + \nabla \cdot \mathbf{F}^{\text{inv}}(Q) - \nabla \cdot \mathbf{F}^{\text{av}}(Q, \mathbf{R}) = G(Q) \end{cases}. \tag{19}$$

Herein, $\mathbf{R}$ is the auxiliary variable used to facilitate the discretization of viscous fluxes.

The artificial viscosity ε is modeled following the approach by Persson and Peraire (2006). Several modifications are introduced to make this model more suitable for sharp thermal front capturing in nonhydrostatic atmospheric modeling. In this study, the resolution-based indicator is used to detect nonsmooth flow features. Specifically, we approximate the solution in the polynomial space $\mathbb{Q}^k(\Omega)$ as follows:

$$Q \approx U = \sum_{i=1}^{N(k)} U_i \phi_i, \tag{20}$$

where U is the polynomial approximation of Q, ϕ_i is the ith basis of the space $\mathbb{Q}^k(\Omega)$, and $N(k)$ is the total number of basis of $\mathbb{Q}^k(\Omega)$; for two-dimensional problems, $N(k) = (k+1) \times (k+1)$.

Now we project the solution U onto the polynomial space $\mathbb{Q}^{k-1}(\Omega)$, and obtain

$$U^p = \sum_{i=1}^{N(k-1)} \hat{U}_i \hat{\phi}_i. \tag{21}$$

Herein, $\hat{\phi}_i$ is the ith basis of the space $\mathbb{Q}^{k-1}(\Omega)$, and $\hat{U}_i$ is the corresponding expansion coefficient. The expansion coefficients can be calculated by solving the following linear system:

$$\sum_{m=1}^{N(k-1)} \hat{U}_m \langle \hat{\phi}_m, \hat{\phi}_j \rangle = \sum_{m=1}^{N(k)} U_m \langle \phi_m, \hat{\phi}_j \rangle, \quad j = 1, \ldots, N(k-1). \tag{22}$$

Note that $\langle \cdot, \cdot \rangle$ indicates the inner product in $L^2(\Omega)$.

The resolution-based indicator in one finite element can then be defined as

$$S_e = \log_{10} \frac{\langle U - U^p, U - U^p \rangle_e}{\langle U, U \rangle_e}. \tag{23}$$

In case that $\langle U, U \rangle_e = 0$ or $U = U^p$, S_e is directly set as -100 when $\langle U - U^p, U - U^p \rangle_e < 10^{-16}$. Clearly, if $\langle U, U \rangle_e = 0$, then $U = U^p = 0$, and thus $\langle U - U^p, U - U^p \rangle_e < 10^{-16}$; if $U = U^p$, then $\langle U - U^p, U - U^p \rangle_e < 10^{-16}$. For both cases, the smooth indicator S_e is directly set as -100.

Finally, a smooth variation of the element-wise artificial viscosity ε_e is reconstructed as follows:

$$\varepsilon_e = \begin{cases} 0 & \text{if} \quad S_e < S_0 - \kappa \\ \dfrac{\varepsilon_0}{2}\left[1 + \sin\dfrac{\pi(S_e - S_0)}{2\kappa}\right] & \text{if} \quad S_0 - \kappa \le S_e \le S_0 + \kappa \\ \varepsilon_0 & \text{if} \quad S_e > S_0 + \kappa \end{cases}. \tag{24}$$

Herein, ε_0 is the magnitude of the artificial viscosity, S_0 is the estimated value of the smoothness indicator S_e for smooth flow features, and κ is the control parameter of the smoothness range. From Eq. (24), it is clear that $\varepsilon_e \in [0, \varepsilon_0]$. According to Persson and Peraire (2006), if the polynomial expansion has a similar behavior to the Fourier expansion, the smoothness indicator will be proportional to $-4\log_{10}(k)$. Based on our analyses, this estimate can add unnecessary numerical dissipation to relatively smooth flow features. Therefore, S_0 is set as $-3\log_{10}(k)$ in this study. The parameter κ determines the smoothness range on which the artificial viscosity functions. Generally, κ needs to be chosen sufficiently large so as to ensure a sharp front capturing with smooth transition to flow fields nearby. It is found that κ affects the performance of artificial viscosity more than the other parameters in Eq. (24). More test results on this parameter will be discussed in the following section.

In contrast to the modeling approach presented by Persson and Peraire (2006), the artificial viscosity ε_0 is modeled as follows. First we introduce several notations. Let U, L, and α be the characteristic speed of the flow, the characteristic length, and the diffusion coefficient. Then, the Pèclet number Pe for a diffusion process can be given by

$$\mathrm{Pe} = \frac{LU}{\alpha}. \tag{25}$$

We will use it afterward. Note that the parameter definitions here are different from those in the work by Persson and Peraire (2006), and Barter and Darmofal (2010). In those works, the concept of the Pèclet number is not introduced. To model the artificial viscosity ε_0, the characteristic speed of the flow U and the characteristic length L are used to match the dimension. Specifically, U is set as the maximum absolute value of the characteristic speed $|\lambda|_{\max}$, and L is the subcell grid size h/P, where h is the element size and P is the polynomial order.

In this work, the artificial viscosity ε_0 is allowed to be proportional to α. Different models to bridge ε_0 and α are proposed to make the modeling of the artificial viscosity ε_0 less sensitive to the element size and polynomial order. The principles followed in this approach include the following:

- the artificial viscosity ε_0 is nonnegative;
- when the resolution of the numerical scheme is infinite, the artificial viscosity $\varepsilon_0 \to 0$; and
- the modeling is compatible with the classic results from the second-order accurate (or equivalently P^1 reconstruction) methods.

Instead of using the uniform assumption of the subcell grid size h/P, we redefine the length scale in Eq. (25) as the maximum distance between two adjacent quadrature points in the element, which is written as $\Delta h_{\max} = \Delta\xi_{\max} h$, where $\Delta\xi_{\max}$, scaled in [0, 1], is the maximum distance between two adjacent quadrature points in a standard one-dimensional element. Following the literature by Barter and Darmofal (2010), the characteristic speed of the flow U is taken as $|\lambda|_{\max}$. As a result, α reads

$$\alpha = \frac{\Delta\xi_{\max}}{\mathrm{Pe}} h |\lambda|_{\max}. \tag{26}$$

A general model for the artificial viscosity ε_0 can then be written as

$$\varepsilon_0 = f(\Delta\xi_{\max}) h |\lambda|_{\max}. \tag{27}$$

We now focus on the modeling of the nondimensional function $f(\Delta\xi_{\max})$. Following the work by Huang et al. (2005), we require that when the P^1 reconstruction is

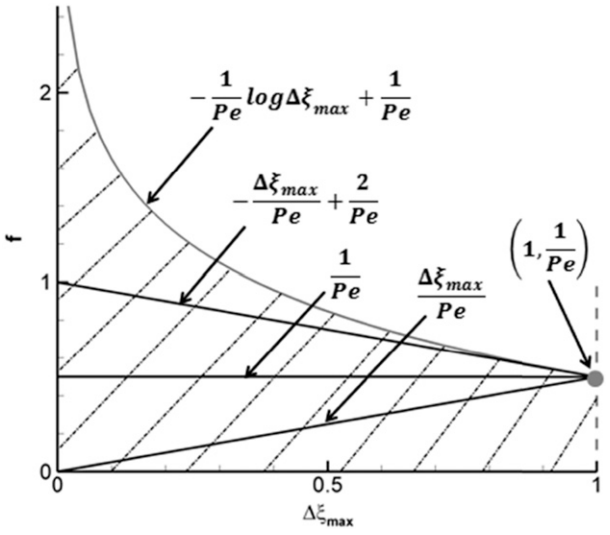

FIG. 1. Paradigm of the family of functions $f(\Delta\xi_{\max})$ in the artificial viscosity model.

used, the function f passes the point $(1, \mathrm{Pe}^{-1})$. This is consistent with the definition of α for the second-order finite-volume method. Then we show one approach to determine a region of the function f that can satisfy the proposed modeling criteria. It is observed that one possible upper bound of the function f can be written as

$$f(\Delta\xi_{\max}) = -\frac{1}{\mathrm{Pe}}\log\Delta\xi_{\max} + \frac{1}{\mathrm{Pe}}, \quad \Delta\xi_{\max} \in [0,1]. \tag{28}$$

It is not difficult to verify that $f(\Delta\xi_{\max}) > 0$; if $\Delta\xi_{\max} h \to 0$, then $\varepsilon_0 \to 0$; and $f(\Delta\xi_{\max})$ passes the point $(1, \mathrm{Pe}^{-1})$. One possible lower bound of the function f can be expressed as

$$f(\Delta\xi_{\max}) = \begin{cases} 0, & 0 \le \Delta\xi_{\max} < 1 \\ \dfrac{1}{\mathrm{Pe}}, & \Delta\xi_{\max} = 1 \end{cases}. \tag{29}$$

This region is shown as the shadowed area in Fig. 1. Note that the linear function $f(\Delta\xi_{\max}) = \Delta\xi_{\max}/\mathrm{Pe}$ recovers the choice by Persson and Peraire (2006) and Barter and Darmofal (2010). Based on our tests, the linear distribution

$$f(\Delta\xi_{\max}) = -\frac{\Delta\xi_{\max}}{\mathrm{Pe}} + \frac{2}{\mathrm{Pe}} \tag{30}$$

is used to relate ε_0 with α. Finally, the artificial viscosity ε_0 is defined as

$$\varepsilon_0 = \left(-\frac{\Delta\xi_{\max}}{\mathrm{Pe}} + \frac{2}{\mathrm{Pe}}\right) h|\lambda|_{\max}. \tag{31}$$

From Eq. (31) and also Fig. 1, it is observed that when h is held as a constant value and $\Delta\xi_{\max}$ is reduced toward zero, the artificial viscosity ε_0 does not decrease to zero. But when the grid size is infinitesimally small, the artificial viscosity ε_0 approaches zero as required by Eq. (31). A physically sound way to interpret this new family of artificial viscosity goes as follows. To capture the flow discontinuity, one does not expect that the polynomial order be increased substantially (i.e., $\Delta\xi_{\max}$ is decreased substantially toward zero). Instead, the polynomial order is fixed (i.e., $\Delta\xi_{\max}$ is fixed), and the grid will be substantially refined near the flow discontinuity. This indicates that the grid size h is expected to decrease toward zero for flow discontinuity capturing. As a result, the artificial viscosity ε_0 will decrease to zero as indicated by Eq. (31).

We note that the artificial viscosity ε_e given in Eq. (24) is an element-wise constant distribution. It is obvious that ε_e has a jump on element interfaces if the element-wise constant distribution is used. For quadrilateral elements, a bilinear distribution can be constructed by interpolating the four vertex artificial viscosity values to the desired quadrature points. The value of artificial viscosity on a specific vertex is calculated by averaging all values from the neighboring elements that share the vertex.

It is also noted that when the numerical resolution is sufficiently high, the localized Laplacian artificial viscosity will be deactivated. As a result, the convergence rate of the numerical scheme will not be affected. If the localized Laplacian artificial viscosity is activated, the convergence rate of the numerical scheme will be affected by the percentage of elements that are marked off by the smoothness indicators. When the numerical resolution is low, the localized Laplacian artificial viscosity will be activated in a large portion of the flow fields. As a result, the convergence rate of the numerical scheme will be lower than the optimal one. As the numerical resolution increases, the localized Laplacian artificial viscosity will be occasionally activated in a small portion of the flow fields. Consequently, the numerical error is found to be substantially reduced comparing with that of the low-resolution case. As a result, the convergence rate will be enhanced.

4. Results and discussion

In this section, we test the localized Laplacian artificial viscosity method using several benchmark problems with the presence of shock waves or sharp thermal fronts. The benchmark test cases are summarized as follows:

- Shock capturing for the 1D Burger's equation;
- 1D shock–entropy wave interaction,
- 2D shock–vortex interaction,
- 2D rising thermal bubble, and
- 2D density current.

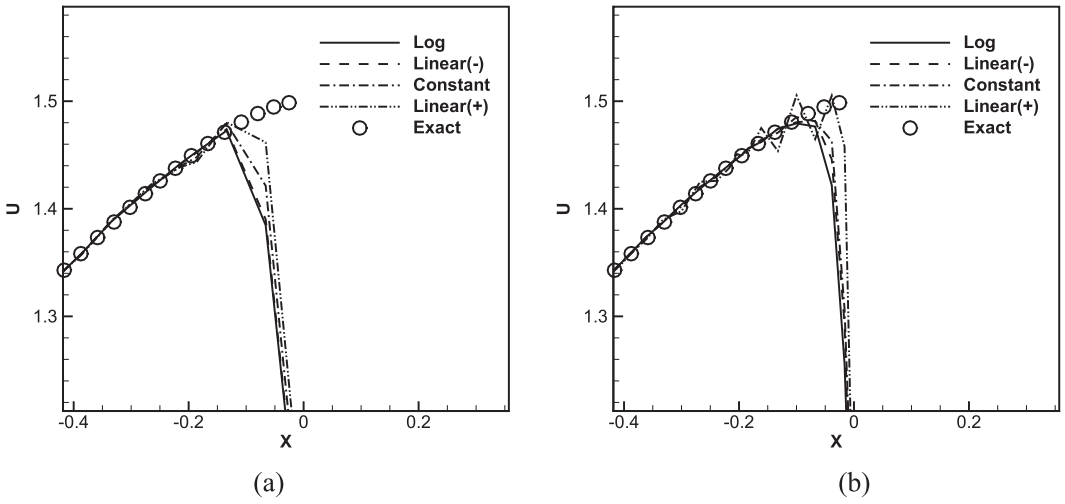

FIG. 2. Zoom-in view of the solutions of the one-dimensional Burger's equation near the shock wave with different artificial viscosity models at $t = 1$ on 10 elements: (a) P^3 reconstruction and (b) P^8 reconstruction.

These test cases are used to demonstrate that the proposed localized Laplacian artificial viscosity method can effectively resolve both flow discontinuity and sharp fronts while not dissipating smooth flow features. The impact of localized Laplacian artificial viscosity on nonhydrostatic atmospheric flow features is investigated in detail using the two-dimensional thermal bubble and density current problem. More verification studies on the sharp shock-capturing capability of the proposed localized Laplacian artificial viscosity method, and the performance comparison with other artificial diffusivity methods and those using limiters can be found by Yu and Wang (2014) and Park et al. (2014).

To evaluate the performance of artificial viscosity on grids with different resolution, a wide range of grid sizes and polynomial orders is tested in each problem. In all simulations, S_0 in Eq. (24) is selected as $-3\log_{10}(k)$ and the Pèclet number Pe is fixed at 2. Based on a large number of flow simulation tests, it is found that $\kappa = 4.0$ robustly work for sharp front capturing, and even for the problems with strong shock waves (Yu and Wang 2014). We note that since the free parameters in the localized Laplacian artificial viscosity are modeled based on both physical criteria and numerical features of the DG discretization, no parameter tuning is required. A caveat is that to achieve the best possible performance of

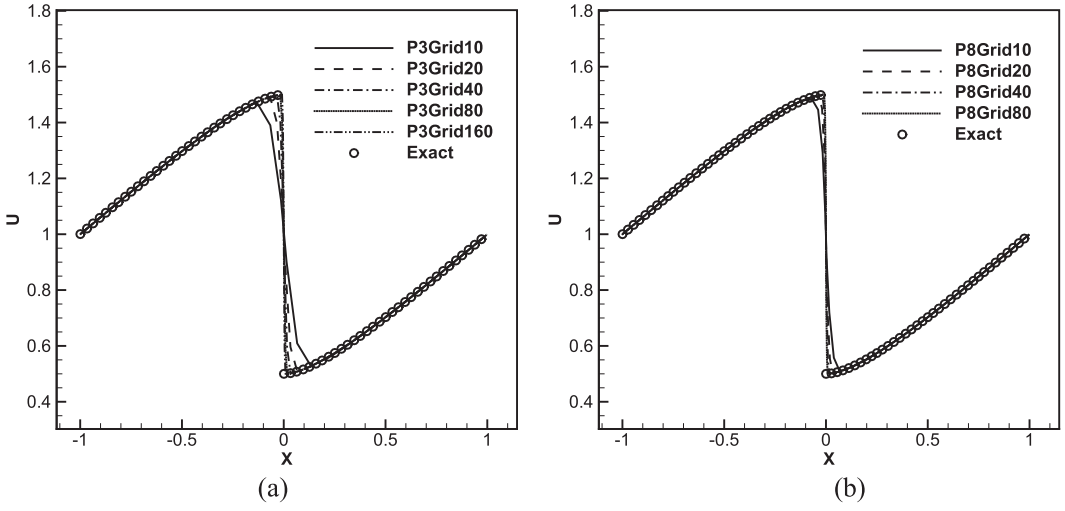

FIG. 3. Solutions of the one-dimensional Burger's equation at $t = 1$ on different grids: (a) P^3 reconstruction and (b) P^8 reconstruction.

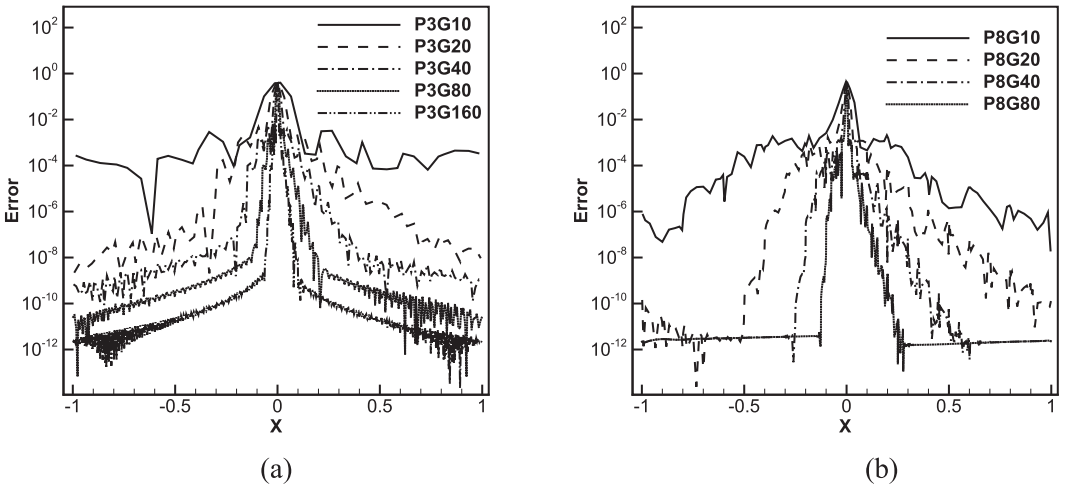

FIG. 4. Local error of computed solutions of the one-dimensional Burger's equation at $t = 1$ on different grids: (a) P^3 reconstruction and (b) P^8 reconstruction.

localized Laplacian artificial viscosity, the free parameters can be slightly adjusted for different flow problems. As discussed in section 3, the parameter κ, which indicates to what extent the flow features are deemed as nonsmooth, affects the performance of artificial viscosity more than the other parameters. As a result, this parameter will be slightly adjusted among different flow problems for the purpose of the best flow resolution. Meanwhile, in order to quantitatively judge the effect of the localized Laplacian artificial viscosity on nonhydrostatic mesoscale atmospheric modeling, we intentionally vary κ in the range of [0.25, 6] for benchmark atmospheric flow tests.

a. One-dimensional and two-dimensional benchmarks involving shock waves

1) ONE-DIMENSIONAL BURGER'S EQUATION TESTS

In this section, we test the efficacy of the localized Laplacian artificial viscosity for the one-dimensional Burger's equation. The one-dimensional inviscid Burger's equation augmented by an artificial diffusive term reads as follows:

$$\frac{\partial U}{\partial t} + \frac{\partial}{\partial x}\left(\frac{1}{2}U^2\right) + \frac{\partial}{\partial x}\left(\varepsilon_e \frac{\partial U}{\partial x}\right) = 0, \tag{32}$$

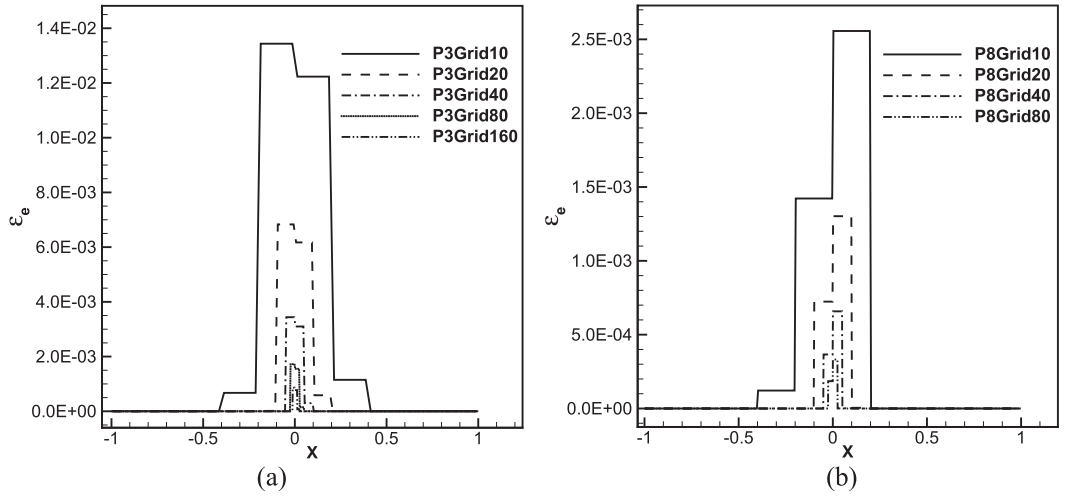

FIG. 5. Distribution of the artificial viscosity from the one-dimensional Burger's equation simulation at $t = 1$ on different grids: (a) P^3 reconstruction and (b) P^8 reconstruction.

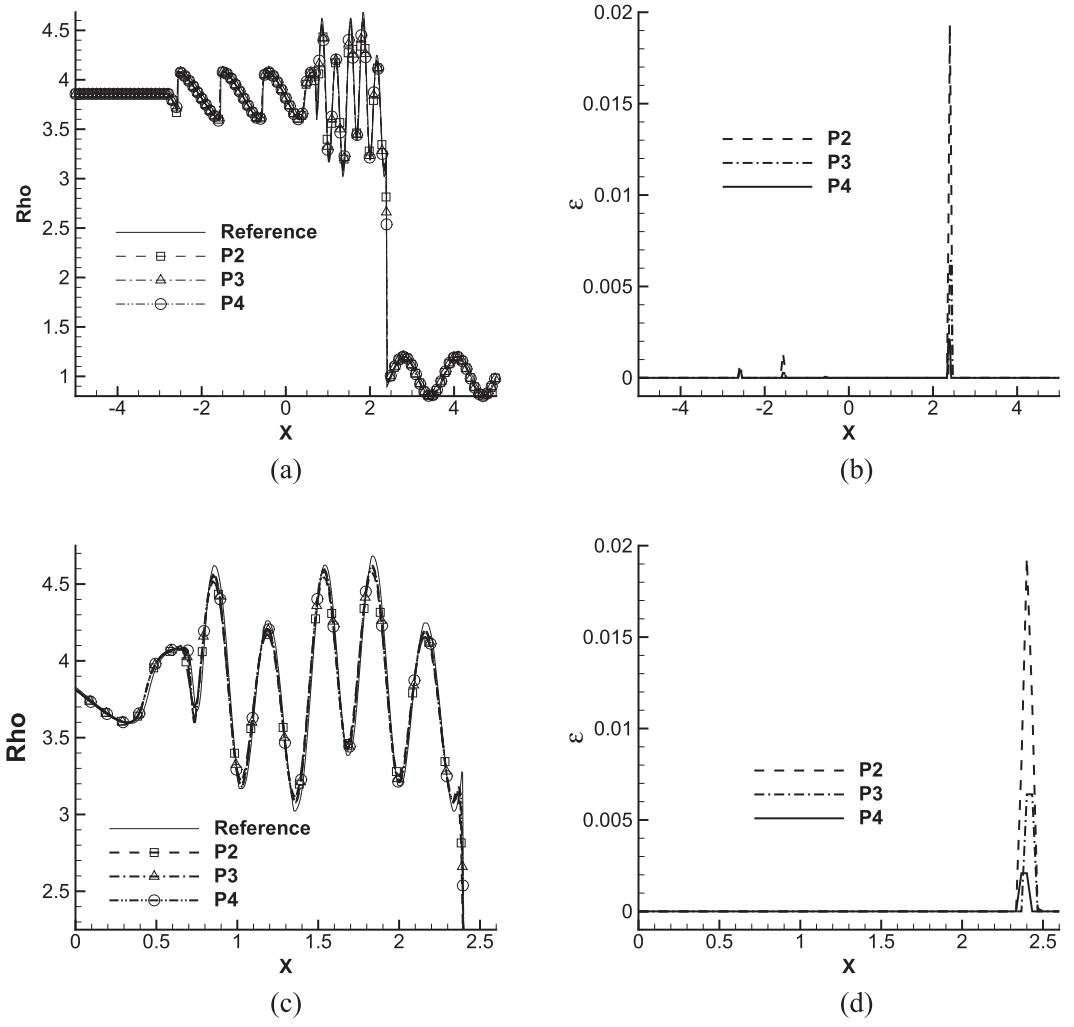

FIG. 6. Density and artificial viscosity distribution at $t = 1.8$ s for the shock–entropy wave interaction problem using $P^2 \sim P^4$ reconstruction. (a) Overview of the density distribution, (b) overview of the artificial viscosity distribution, (c) zoom-in view of the density distribution after the shock wave, and (d) zoom-in view of the artificial viscosity distribution after the shock wave.

where $x \in [-1, 1]$. Periodic boundary conditions are enforced at $x = -1$ and $x = 1$. The initial conditions are defined as $U(x, 0) = U_0(x) = 1 + \sin(\pi x)/2$. According to Harten et al. (1987), a moving shockwave will develop after $t = 2/\pi$ under the given initial conditions. An element-wise constant distribution of ε_e is used to stabilize the shock wave. In all simulations presented in this section, κ is chosen as 6.

First of all, the results of different artificial viscosity models presented in section 3 are compared. The results are shown in Fig. 2. In Fig. 2, ''Log'' denotes the case with $f(\Delta\xi_{\max}) = (1 - \log\Delta\xi_{\max})/\text{Pe}$, ''Linear(−)'' denotes the case with $f(\Delta\xi_{\max}) = (2 - \Delta\xi_{\max})/\text{Pe}$, ''Constant'' denotes the case with $f(\Delta\xi_{\max}) = 1/\text{Pe}$, and "Linear(+)" denotes the case with $f(\Delta\xi_{\max}) = \Delta\xi_{\max}/\text{Pe}$. Simulations with both P^3 and P^8 reconstructions on 10 elements are carried out. From Fig. 2, we observe that the model Log is the most dissipative method and the model Linear(+) is the least dissipative. It is also clear that the performance of the model Linear(+) is sensitive to the polynomial order, while that of the other models is not. The performance of the model Constant is similar to that of the model Linear(+) for the P^3 reconstruction, and similar to that of the model Linear(−) for the P^8 reconstruction. But small oscillations show up near the shock region for both cases with the Constant model. Based on these observations, the model Linear(−) will be used exclusively in all simulations for the rest of the paper.

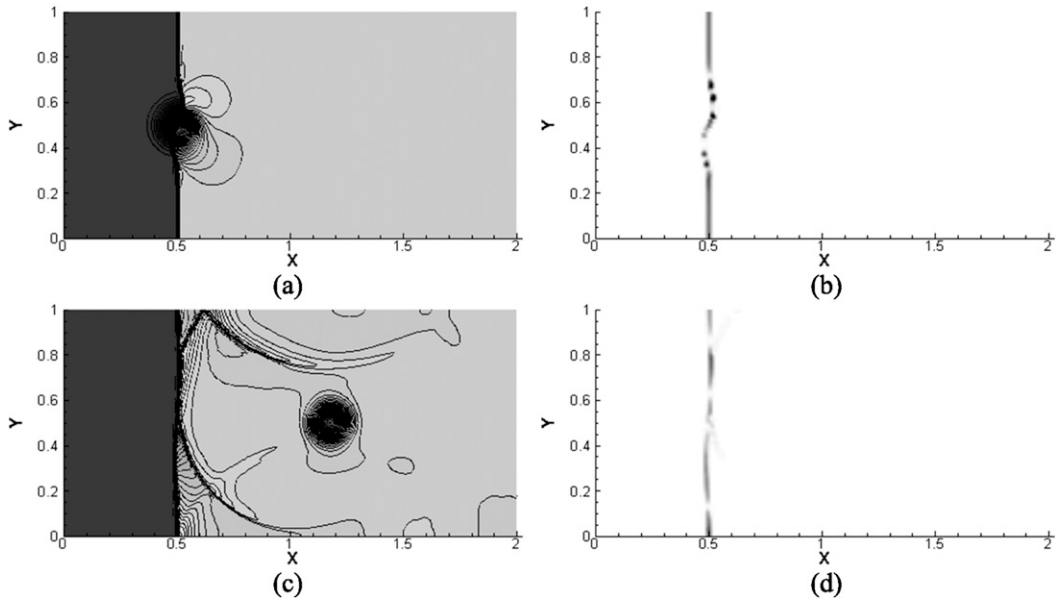

FIG. 7. Pressure (60 equally spaced contour lines from 0.9 to 1.33) and artificial viscosity (60 equally spaced contour lines from 0 to 5×10^{-3}) distribution at $t = 0.2$ and $t = 0.8$ s for the shock–vortex interaction problem using P^2 reconstruction. (a) Density distribution at $t = 0.2$ s, (b) artificial viscosity distribution at $t = 0.2$ s, (c) density distribution at $t = 0.8$ s, and (d) artificial viscosity distribution at $t = 0.8$ s.

Next we compare the results with P^3 and P^8 reconstruction on different grids. The solutions at $t = 1$ are presented in Fig. 3. The corresponding local solution errors with respect to the exact solution of the inviscid Burger's equation and the distribution of artificial viscosity at $t = 1$ are plotted in Figs. 4 and 5, respectively. Several observations are summarized as follows. From Fig. 3, we find that the localized Laplacian artificial viscosity works robustly for a wide range of high-order reconstruction (e.g., from P^3 to P^8 in the current test). For all cases, the shock is sharply captured at the boundary of two adjacent elements. From Figs. 4 and 5, it is clear that the localized Laplacian artificial viscosity does not contaminate the smooth flow features away from the shock, but concentrates in the nonsmooth flow regions to suppress the Gibbs oscillation. From Fig. 5, we observe that as the resolution of the numerical scheme becomes finer (i.e., the element size becomes smaller or the order of the reconstruction polynomial becomes higher), the amount of artificial viscosity localized in the vicinity of the shock wave becomes smaller. This obeys the modeling rules as stated in section 3.

2) ONE-DIMENSIONAL SHOCK–ENTROPY WAVE INTERACTION

The interaction between a shock and an entropy wave, or the Shu–Osher problem (Shu and Osher 1989), is simulated in this section. The initial profile is given as follows:

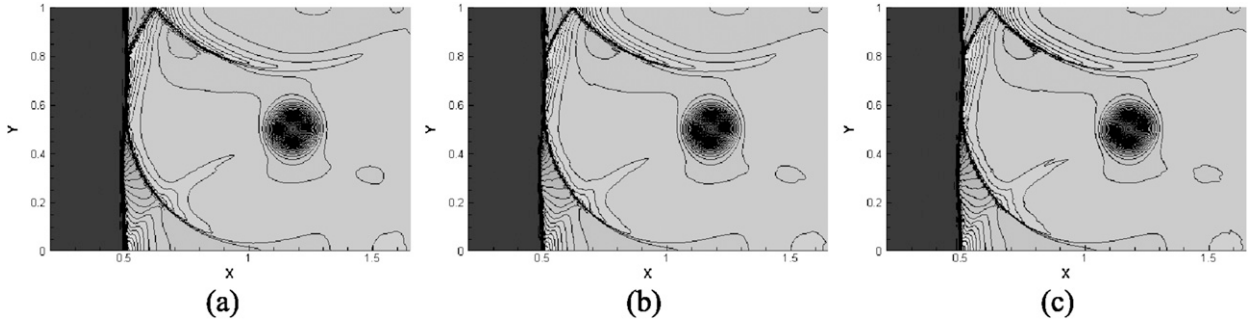

FIG. 8. Pressure distribution at $t = 0.8$ s for the shock–vortex interaction problem using $P^2 \sim P^4$ reconstruction: (a) P^2 reconstruction, (b) P^3 reconstruction, and (c) P^4 reconstruction.

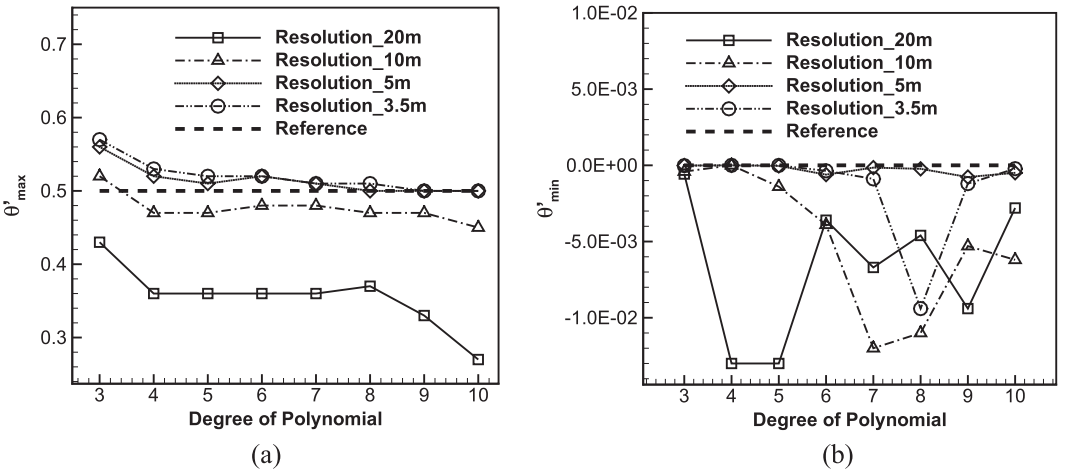

FIG. 9. The maximum and minimum potential temperature perturbations $\theta'_{\max}$ and $\theta'_{\min}$ of the rising thermal bubble at $t = 700$ s with various flow field resolutions: (a) $\theta'_{\max}$ vs degree of polynomial and (b) $\theta'_{\min}$ vs degree of polynomial.

$$\begin{cases}(\rho_L, u_L, p_L) = (3.857\,143, 2.629\,369, 10.3333) & \text{if} \quad x < -4 \\ (\rho_R, u_R, p_R) = [1 + 0.2\sin(5x), 0.0, 1.0] & \text{if} \quad x \geq -4 \end{cases}. \tag{33}$$

The computational domain is $[-5, 5]$ and is divided into 300 elements. The simulation is carried out until $t = 1.8$ s. In this case, an element-wise linear distribution of artificial viscosity is adopted. In all simulations presented in this section, κ is chosen as 4.

The density distribution and the corresponding artificial viscosity distribution at $t = 1.8$ s using different reconstruction accuracy, namely, degrees 2–4, are displayed in Fig. 6. The overview of the results is presented in Figs. 6a and 6b. It is clear that the localized Laplacian artificial viscosity method can sharply capture the interaction between the shock wave and the entropy wave, and the artificial viscosity only concentrates on flow discontinuities. Note that a large amount of artificial viscosity is concentrated at the shock location around $x = 2.5$. Besides, there exists a small amount of artificial viscosity near $x = -2.5$ and $x = -1.5$ to stabilize the density oscillation with sharp gradients. From the enlarged view as shown in Figs. 6c and 6d, it is observed that the localized Laplacian artificial viscosity method can accurately resolve high-frequency entropy waves for all reconstructions of different orders of accuracy. It is also found that as the reconstruction order is increased, better resolution of flow features is obtained.

3) TWO-DIMENSIONAL SHOCK–VORTEX INTERACTION

This test case describes the interaction between a stationary shock wave and a propagating isentropic vortex (Jiang and Shu 1996). The computational domain is $[0, 2] \times [0, 1]$, and is tessellated with uniform elements of size $1/100$. A stationary shock with a preshock Mach number of $M_s = 1.1$ is positioned at $x = 0.5$. Its upstream state is $(\rho_L, u_L, v_L, p_L) = (1.0, M_s\sqrt{\gamma}, 0.0, 1.0)$. The right quantities are calculated from the left ones using jump conditions. An isentropic vortex is superposed to the flow left to the shock and centers at $(x_c, y_c) = (0.25, 0.5)$ with the following flow conditions:

$$v_\theta = \varepsilon\tau e^{\alpha(1-\tau^2)}, \quad \rho = \left(1 - \frac{\gamma - 1}{4\alpha\gamma}\varepsilon^2 e^{2\alpha(1-\tau^2)}\right)^{1/(\gamma-1)}, \quad p = \rho^\gamma, \tag{34}$$

with $\tau = r/r_c$ and $r = \sqrt{(x - x_c)^2 + (y - y_c)^2}$. Herein, v_θ is the circumferential velocity, ε is the strength of the vortex, α is the decay rate of the vortex, and r_c is the critical radius for which the vortex has the maximum strength. In this study, these parameters are set as $\varepsilon = 0.3$, $\alpha = 0.204$, and $r_c = 0.05$. Simulation is carried out until $t = 0.8$ s. In this case, an element-wise linear distribution of artificial viscosity is adopted, with κ chosen as 4.

Pressure distribution and the corresponding artificial viscosity distribution at $t = 0.2$ s and $t = 0.8$ s for P^2 reconstruction are presented in Fig. 7. The pressure contour has 60 equally distributed levels from 0.9 to 1.33. The artificial viscosity contour has 60 equally distributed levels from 0 to 5×10^{-3}. It is clear from Figs. 7b and 7d that the artificial viscosity is localized in the vicinity of the shock, and does not affect the smooth propagating vortex during the entire flow field development process. Comparison of pressure contours at $t = 0.8$ s using different reconstruction accuracy, namely,

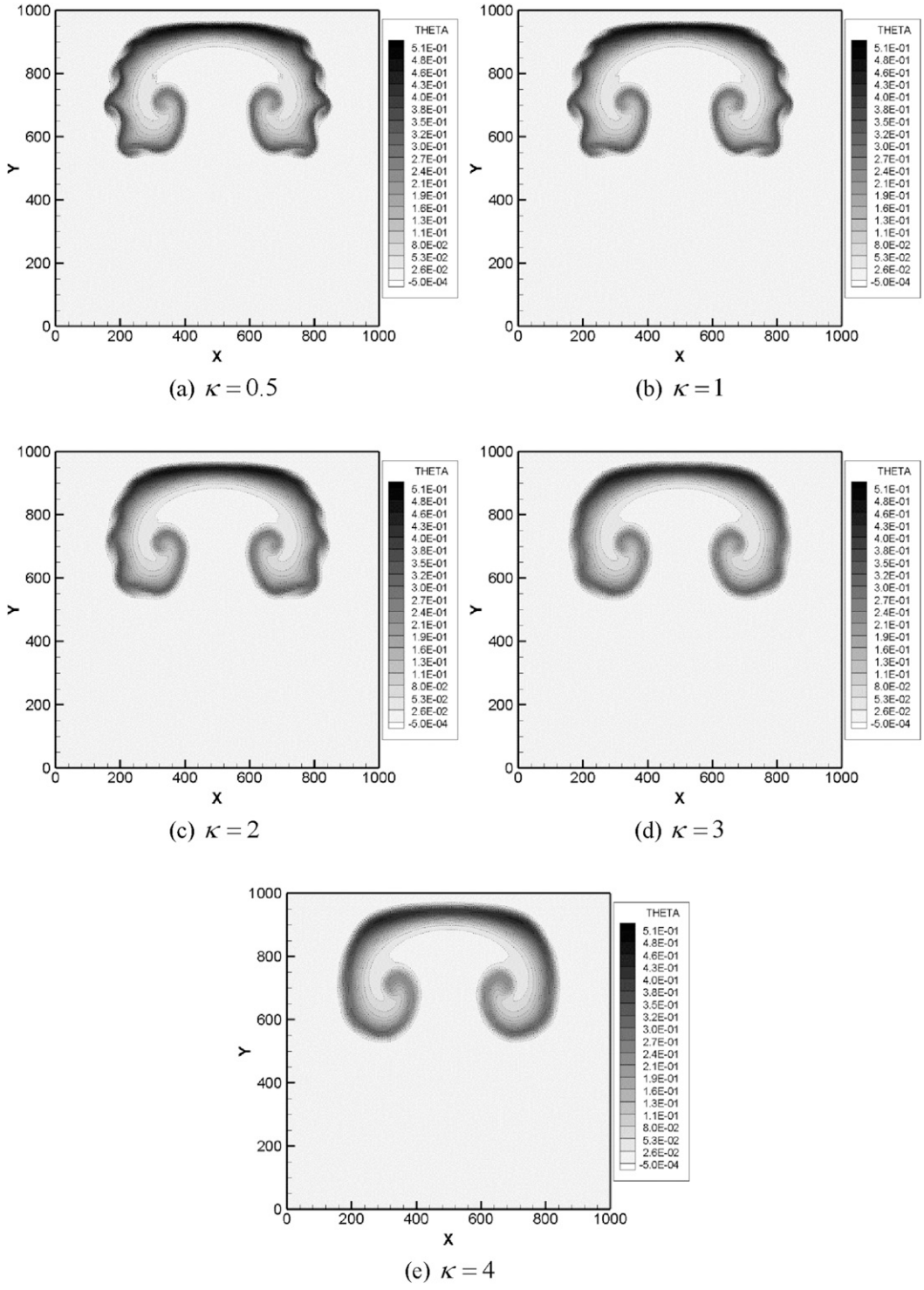

FIG. 10. Potential temperature perturbation fields of the rising thermal bubble at $t = 700$ s for different κ with P^{10} reconstruction on the 20×20 mesh.

degrees 2–4, is presented in Fig. 8. Similarly to the observation in section 4a(2), better resolution of flow features is obtained as the reconstruction order is increased.

b. *Rising thermal bubble*

The rising thermal bubble problem is driven by buoyancy effects. Specifically, a dry warm bubble rises in a

TABLE 1. The maximum and minimum potential temperature perturbations θ'_{max} and θ'_{min} of the rising thermal bubble at $t = 700$ s for different κ with P^{10} reconstruction on a 20×20 mesh.

κ	Max θ'	Min θ'
0.5	0.5049	-4.889×10^{-4}
1.0	0.4919	-2.972×10^{-4}
2.0	0.4774	-1.356×10^{-4}
3.0	0.4506	-4.311×10^{-5}
4.0	0.4381	-6.841×10^{-6}

constant potential temperature environment, and interacts with the ambient air during this process. The initial potential temperature perturbation is given as follows (Giraldo and Restelli 2008):

$$\theta' = \begin{cases} 0 & \text{if} \quad r > r_c, \\ \dfrac{\theta_c}{2}\left[1 + \cos\left(\dfrac{\pi r}{r_c}\right)\right] & \text{if} \quad r \le r_c, \end{cases} \tag{35}$$

where $\theta_c = 273.65$ K, $r_c = 250$ m, $r = \sqrt{(x - x_c)^2 + (z - z_c)^2}$, and $(x_c, z_c) = (500, 300)$ m is the initial geometric center of the bubble. The hydrostatic potential temperature θ_0 for this case is 300 K. The simulation domain is $(x, z) \in [0, 1000]^2$ m. The thermal bubble evolves until $t = 700$ s. Four resolutions, namely, 20, 10, 5, and 3.5 m, as presented by Giraldo and Restelli (2008), are adopted in the simulations. The resolution is defined as $L/(n_{grid} \times k)$, where L is the domain size in the x or z direction, n_{grid} is the number of elements in the corresponding direction, and k is the polynomial order. Unless explicitly specified, κ in the artificial viscosity model is set as 0.5 in all simulations presented in this section.

1) RESULTS FROM LOCALIZED LAPLACIAN ARTIFICIAL VISCOSITY

The maximum and minimum potential temperature perturbations θ'_{max} and θ'_{min} at $t = 700$ s with various flow field resolutions are presented in Fig. 9. Note that since initially $\theta' \in [0, 0.5]$, it is then expected that during the evolution of the thermal bubble, θ' is bounded in this range. From Fig. 9, it is found that the localized Laplacian artificial viscosity functions perform well for a wide range of grid sizes and polynomial orders. Only small overshoots of potential temperature perturbation appear in the results. As the resolution of flow fields becomes finer, the numerical dissipation becomes smaller. Correspondingly, both maximum and minimum potential temperature perturbations approach the theoretical bounds.

We now study the effects of κ on flow field features with P^{10} reconstruction on a 20×20 mesh (i.e., the resolution is 5 m). The potential temperature perturbation fields with different κ, namely, 0.5, 1, 2, 3, and 4, are shown in Fig. 10. It is observed that as κ increases, the plumelike flow features near the thermal front are gradually damped. From the maximum and minimum potential temperature perturbations θ'_{max} and θ'_{min} at $t = 700$ s as tabulated in Table 1, it is clear that the overshoot of θ'_{min} for all cases is very small, and decreases quickly as κ increases.

The mass and energy conservation properties are studied for low-resolution cases, including both 20- and 10-m cases. The mass and energy are defined as

$$M(t) = \int_\Omega \rho(t)\, dV \quad \text{and} \quad E(t) = \int_\Omega \rho(t) e(t)\, dV, \tag{36}$$

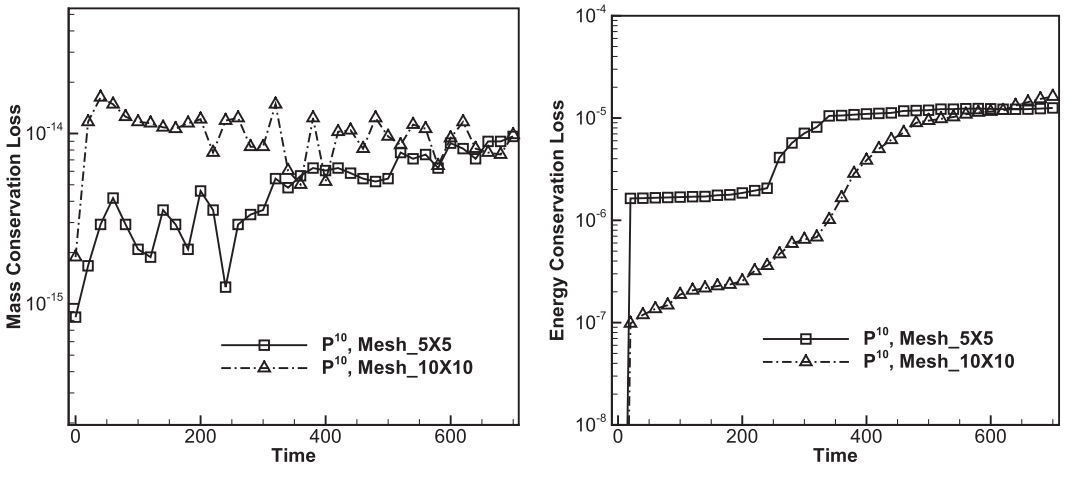

FIG. 11. Conservation of (a) mass and (b) energy for the rising thermal bubble simulations using localized artificial viscosity on two sets of meshes (i.e., 5×5 and 10×10) with P^{10} reconstruction.

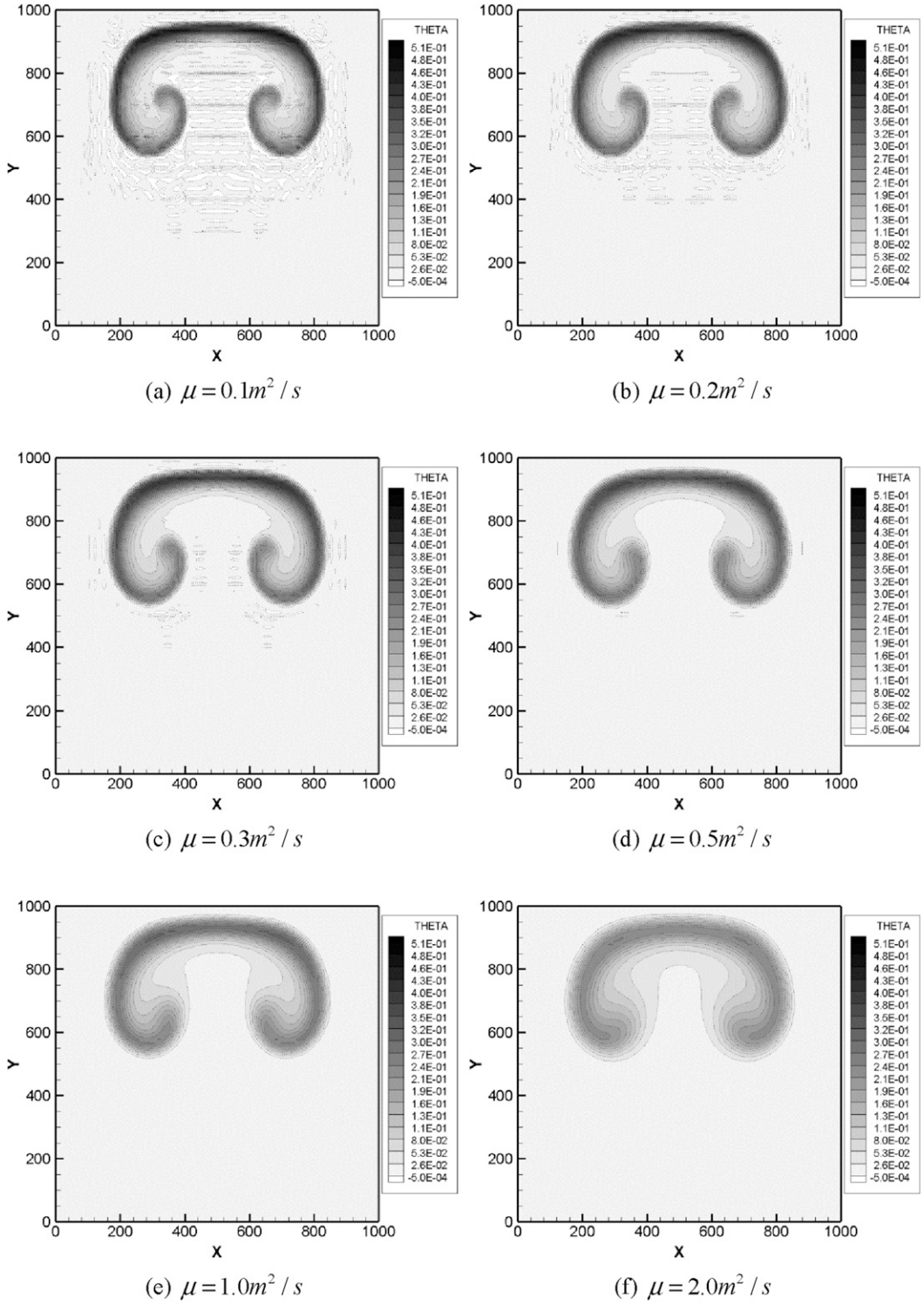

FIG. 12. Potential temperature perturbation fields of the rising thermal bubble at $t = 700$ s for constant viscosity with different μ using P^{10} reconstruction on the 10×10 mesh.

TABLE 2. The maximum and minimum potential temperature perturbations θ'_{max} and θ'_{min} of the rising thermal bubble at $t = 700$ s for localized Laplacian artificial viscosity and constant viscosity with different μ using P^{10} reconstruction on a 10×10 mesh.

	Max θ'	Min θ'
Localized Laplacian artificial viscosity	0.4409	-6.196×10^{-3}
Constant viscosity, $\mu = 0.1\,m^2\,s^{-1}$	0.4828	-4.905×10^{-2}
Constant viscosity, $\mu = 0.2\,m^2\,s^{-1}$	0.4404	-2.115×10^{-2}
Constant viscosity, $\mu = 0.3\,m^2\,s^{-1}$	0.4065	-9.665×10^{-3}
Constant viscosity, $\mu = 0.5\,m^2\,s^{-1}$	0.3611	-1.919×10^{-3}
Constant viscosity, $\mu = 1\,m^2\,s^{-1}$	0.3012	-4.290×10^{-5}
Constant viscosity, $\mu = 2\,m^2\,s^{-1}$	0.2431	-1.655×10^{-9}

where e is the total energy. In this case, e is calculated as $[p/(\gamma - 1)] + (1/2)(u^2 + v^2) + gz$. Correspondingly, the mass and energy conservation loss are defined as

$$M_{\text{Loss}}(t) = \left|\frac{M(t) - M(0)}{M(0)}\right| \quad \text{and} \quad E_{\text{Loss}}(t) = \left|\frac{E(t) - E(0)}{E(0)}\right|. \tag{37}$$

The results for P^{10} solution reconstruction on both 5×5 and 10×10 meshes are shown in Fig. 11. It is found that the localized Laplacian artificial viscosity can ensure mass conservation and only dissipates internal energy, which is expected since the artificial viscosity used here is not meant to represent the proper Navier–Stokes viscous stress terms.

2) COMPARISON BETWEEN LOCALIZED LAPLACIAN ARTIFICIAL VISCOSITY AND CONSTANT VISCOSITY

Currently a common practice to suppress Gibbs oscillation in thermal front capturing is to add constant viscosity (Yelash et al. 2014) to the governing equations. Specifically, the physical viscous diffusion term $\nabla \cdot \mathbf{F}^v(Q, \nabla Q)$ is added to the right-hand side of Eq. (4). The term $\mathbf{F}^v(Q, \nabla Q)$ in the x and z directions can be written as

$$f^v = \begin{pmatrix} 0 \\ \mu\rho\dfrac{\partial u}{\partial x} \\ \mu\rho\dfrac{\partial w}{\partial x} \\ \mu\rho\dfrac{\partial \theta}{\partial x} \end{pmatrix} \quad \text{and} \quad g^v = \begin{pmatrix} 0 \\ \mu\rho\dfrac{\partial u}{\partial z} \\ \mu\rho\dfrac{\partial w}{\partial z} \\ \mu\rho\dfrac{\partial \theta}{\partial z} \end{pmatrix}, \tag{38}$$

where μ is a constant viscosity.

It is obvious that this approach adds numerical dissipation to the entire flow field, no matter whether the local flow features are smooth or not. The potential temperature perturbation fields at 700 s for P^{10} solution reconstruction on a 10×10 mesh using a series of constant viscosity, namely, 0.1, 0.2, 0.3, 0.5, 1, and $2\,m^2\,s^{-1}$, are presented in Fig. 12. The corresponding maximum and minimum potential temperature perturbations θ'_{max} and θ'_{min} at $t = 700$ s using localized Laplacian artificial viscosity and constant viscosity are tabulated in Table 2. Note that the nominal resolution for all the presented results with constant viscosity is 10 m. For comparison purpose, the potential temperature perturbation fields at 700 s for P^{10} solution reconstruction on both 5×5 (i.e., resolution of 20 m) and 10×10 (i.e., resolution of 10 m) meshes using localized Laplacian artificial viscosity with $\kappa = 0.5$ are displayed in Fig. 13. From these results, we observe that for the rising

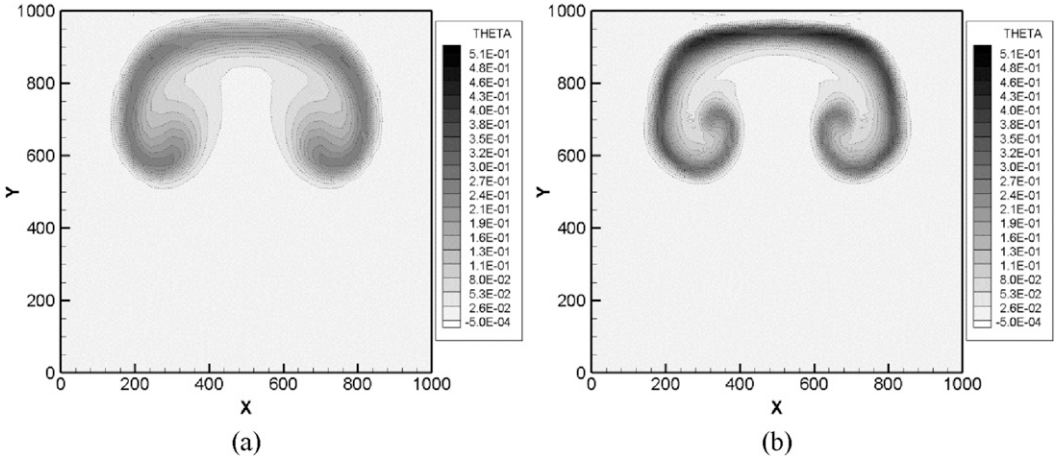

FIG. 13. Potential temperature perturbation fields of the rising thermal bubble at $t = 700$ s for localized artificial viscosity with $\kappa = 0.5$ using P^{10} reconstruction on both (a) 5×5 (i.e., resolution of 20 m) and (b) 10×10 (i.e., resolution of 10 m) meshes.

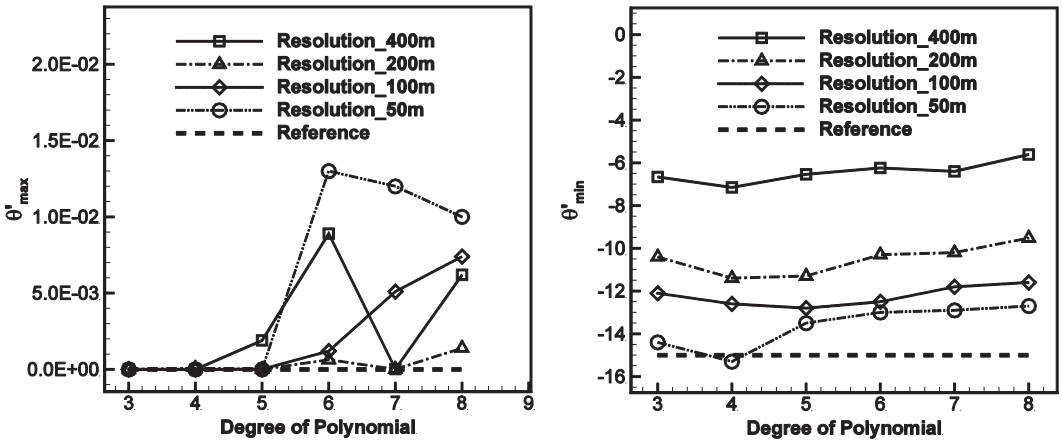

FIG. 14. The maximum and minimum potential temperature perturbations $\theta'_{\max}$ and $\theta'_{\min}$ of the density current flow at $t = 900$ s with various flow field resolutions: (a) $\theta'_{\max}$ vs degree of polynomial and (b) $\theta'_{\min}$ vs degree of polynomial.

thermal bubble case, the performance of constant viscosity with $\mu = 0.2\,\mathrm{m^2\,s^{-1}}$, as presented in Fig. 12b, is very similar to that of localized Laplacian artificial viscosity as shown in Fig. 13b. If the constant viscosity is very large (e.g., $\mu = 2\,\mathrm{m^2\,s^{-1}}$), as shown in Fig. 12f, the flow structures can be severely dissipated. Although a 10×10 mesh is used, the resolution of the case with $\mu = 2\,\mathrm{m^2\,s^{-1}}$ is very similar to the localized Laplacian artificial viscosity case on a 5×5 mesh as show in Fig. 13a. More advantages of the localized Laplacian artificial viscosity approach over the constant viscosity approach will be demonstrated in section 4c(2).

c. *Density current*

Now we study the density current problem. In this case, a cold bubble drops in a neutrally stratified atmosphere, hits the ground, and generates Kelvin–Helmholtz rotors. The initial potential temperature perturbation is given as follows (Giraldo and Restelli 2008):

$$\theta' = \frac{\theta_c}{2}\left[1 + \cos\left(\frac{\pi r}{r_c}\right)\right], \tag{39}$$

where $\theta_c = 258.15\,\mathrm{K}$, $r_c = 1\,\mathrm{m}$, $r = \sqrt{[(x-x_c)/x_r]^2 + [(z-z_c)/z_r]^2}$, $(x_c, z_c) = (0, 3000)\,\mathrm{m}$ is the initial center of the bubble, and $(x_r, z_r) = (4000, 2000)\,\mathrm{m}$. Similarly to the rising thermal bubble case, the hydrostatic potential temperature θ_0 is set to 300 K. The simulation domain is $(x, z) \in [0, 25600] \times [0, 6400]\,\mathrm{m}$. The cold bubble evolves until $t = 900$ s. Four resolutions, namely, 400, 200, 100, and 50 m, are used in the simulations. As discussed by Skamarock and Klemp (2008) and Jebens et al. (2009), flow discontinuities develop quickly in the density current problem for the inviscid Euler equations. In the work by Giraldo and Restelli (2008), a constant dynamic viscosity is used to ensure a grid-converged solution at approximately 50-m resolution. The convergence property of the present flow solver has been demonstrated in previous work (Giraldo and Restelli 2008). In this study, we focus on the solutions for the inviscid Euler equations. The flow feature based localized Laplacian artificial viscosity is used to stabilize the DG discretization near flow discontinuities self-adaptively. Unless explicitly specified, κ in the artificial viscosity model is set as 1 in all simulations presented in this section.

1) RESULTS FROM LOCALIZED LAPLACIAN ARTIFICIAL VISCOSITY

The maximum and minimum potential temperature perturbations $\theta'_{\max}$ and $\theta'_{\min}$ at $t = 900$ s with various flow field resolutions are presented in Fig. 14. Similar conclusions can be drawn from this figure as those for the rising thermal bubble case. The localized Laplacian artificial viscosity works well in a wide range of grid sizes and polynomial orders.

The effects of κ on flow field features are studied with P^8 reconstruction on both 8×2 (i.e., 400-m resolution) and 64×16 meshes (i.e., 50-m resolution). The potential temperature perturbation fields with different κ, namely, 0.25, 0.5, and 1, on the coarse mesh, and those with $\kappa = 0.5, 1, 2, 4$, and 6 on the fine mesh are displayed in Figs. 15 and 16, respectively. It is found that the artificial viscosity is very dissipative on the coarse mesh, even when a small κ is used. For the fine grid results, as κ increases, fewer Kelvin–Helmholtz rotors are generated. In Table 3, we tabulate the maximum and minimum potential temperature perturbations $\theta'_{\max}$ and $\theta'_{\min}$ at $t = 900$ s for the fine grid results. It is clear from

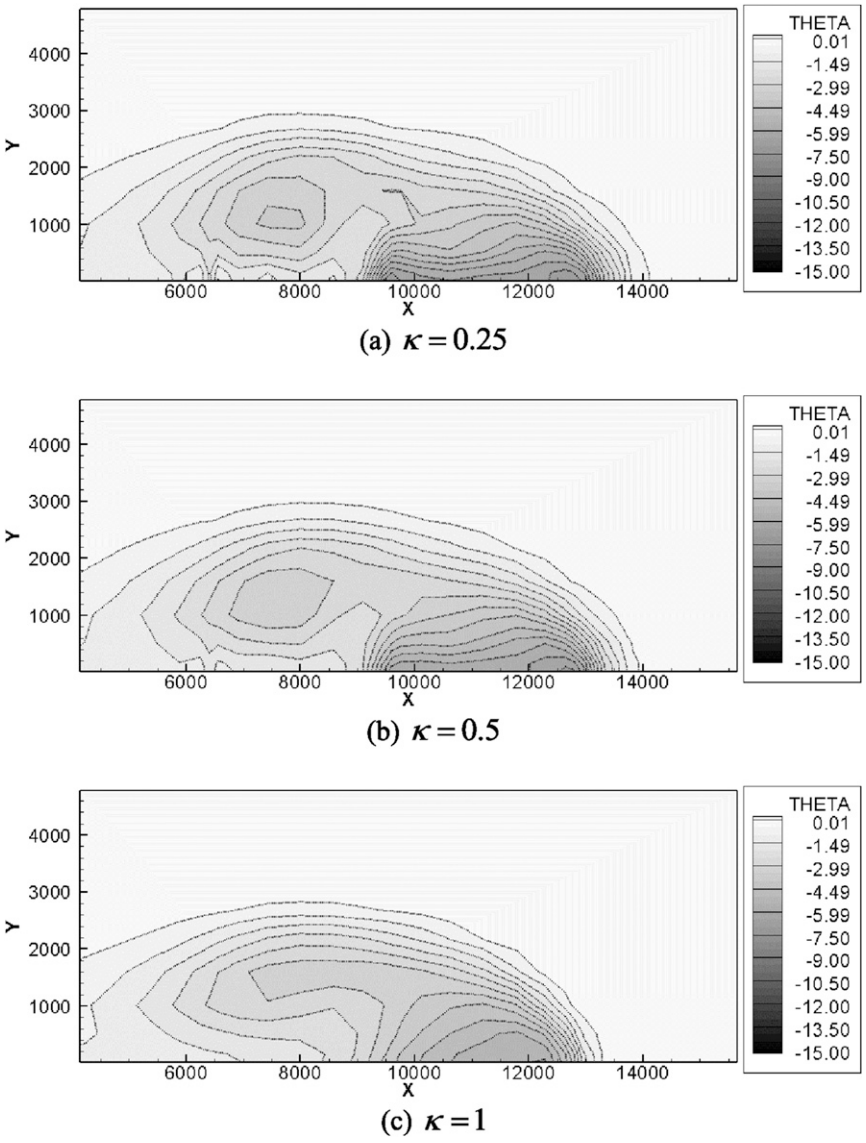

FIG. 15. Potential temperature perturbation fields of the density current at $t = 900$ s for different κ with P^8 reconstruction on the 8×2 mesh. A total of 31 contour levels from -15.00 to 0.01 are used in the figure with every third contour level presented in the legend to avoid it being overly crowded.

Table 3 that the overshoot of $\theta'_{\max}$ for all cases is small, and decreases quickly as κ increases, especially when κ exceeds 2.

2) COMPARISON BETWEEN LOCALIZED LAPLACIAN ARTIFICIAL VISCOSITY AND CONSTANT VISCOSITY

The potential temperature perturbation fields at 900 s for P^8 solution reconstruction on a 16×4 mesh using localized Laplacian artificial viscosity and a series of constant viscosity, namely, 50, 75, 100, and 125 $m^2 s^{-1}$, are displayed in Fig. 17. The corresponding maximum and minimum potential temperature perturbations $\theta'_{\max}$ and $\theta'_{\min}$ at $t = 900$ s using localized Laplacian artificial viscosity and constant viscosity are tabulated in Table 4. A similar trend can be concluded as that in section 4b(3).

It is found that if the constant viscosity is "small" (e.g., $\mu = 25\,m^2 s^{-1}$) the simulation diverged. Note that $\mu = 2\,m^2 s^{-1}$ is considered as a "large" viscosity value in the rising thermal bubble case. Thus, one drawback of the constant viscosity approach is that the selection of the stabilization viscosity parameter is largely problem dependent. In contrast, the value of localized Laplacian

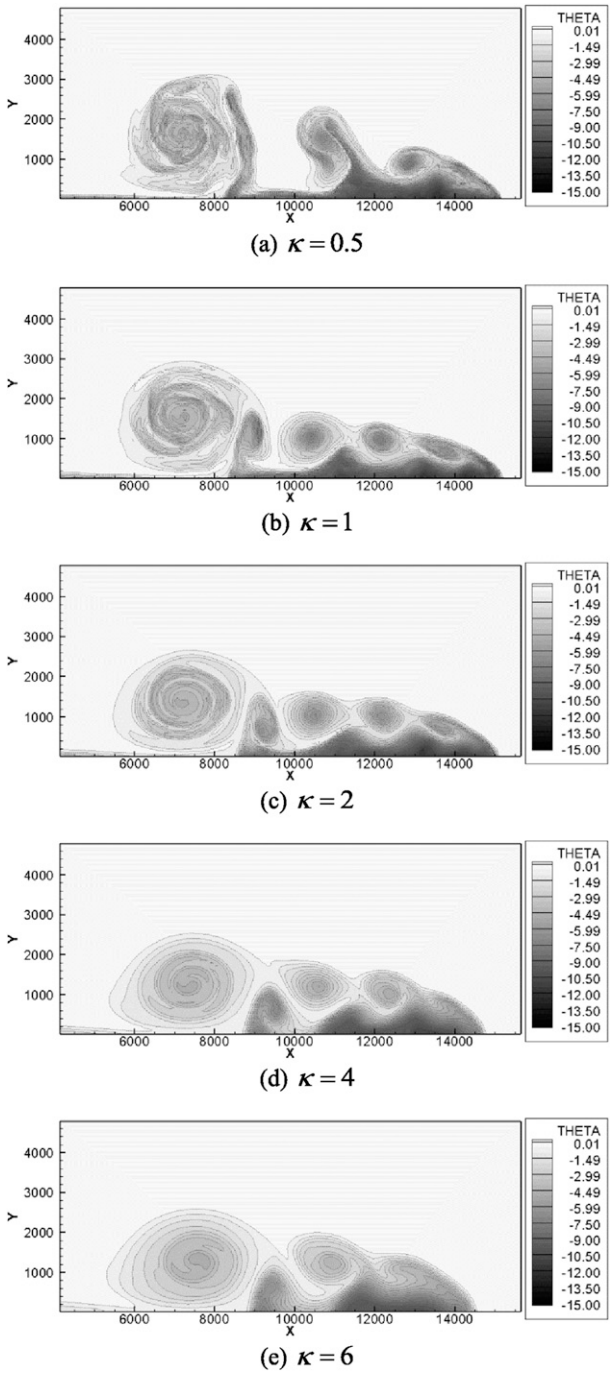

FIG. 16. Potential temperature perturbation fields of the density current at $t = 900$ s for different κ with P^8 reconstruction on a 64×16 mesh. A total of 31 contour levels from -15.00 to 0.01 are used in the figure with every third contour level presented in the legend to avoid it being overly crowded.

artificial viscosity is automatically determined from the design mechanism considering key factors such as the smoothness of the flow field and the numerical resolution of the scheme, and no parameter adjustment is needed in simulations of different problems. This appears to be one big advantage of the localized Laplacian artificial viscosity over the constant viscosity approach.

TABLE 3. The maximum and minimum potential temperature perturbations $\theta'_{\max}$ and $\theta'_{\min}$ of the density current at $t = 900$ s for different κ with P^8 reconstruction on a 64×16 mesh.

κ	Max θ'	Min θ'
0.5	1.425×10^{-2}	-13.59
1.0	7.743×10^{-3}	-14.60
2.0	4.007×10^{-4}	-12.17
4.0	4.740×10^{-8}	-11.03
6.0	2.457×10^{-8}	-10.33

5. Summary and outlook

We present a flow-feature-based localized Laplacian artificial viscosity method for DG discretization of nonhydrostatic mesoscale atmospheric modeling. This method can effectively suppress Gibbs oscillation near sharp thermal fronts, while not affecting smooth flow features elsewhere. Specifically, the original inviscid governing equations are augmented by localized Laplacian artificial diffusive terms. The diffusivity is a function of the local smoothness of the flow fields. Thus, the proposed method has a favorable subcell shock capturing property, and does not contaminate the smooth flow features away from the nonsmooth regions. To alleviate the sensitivity of the free parameters in artificial viscosity modeling on both grid sizes and polynomial orders, a family of localized Laplacian artificial viscosity models is proposed based on both physical criteria and numerical features of the DG discretization.

The efficacy of the proposed localized Laplacian artificial viscosity method is then demonstrated by using three one-dimensional and two-dimensional benchmarks involving shock waves, including shock capturing for the one-dimensional Burger's equation, one-dimensional shock–entropy wave interaction, and two-dimensional shock–vortex interaction. Finally, we use the developed numerical framework to simulate two classical two-dimensional test cases from nonhydrostatic mesoscale atmospheric modeling, namely, rising thermal bubble and density current tests. It is found that a fixed set of parameters in artificial viscosity work robustly for both problems with a wide range of grid sizes and polynomial orders. In addition, the artificial viscosity only slightly dissipates total energy but not affects mass conservation. The results using localized Laplacian artificial viscosity are then compared with those using constant viscosity. It is found that for the constant

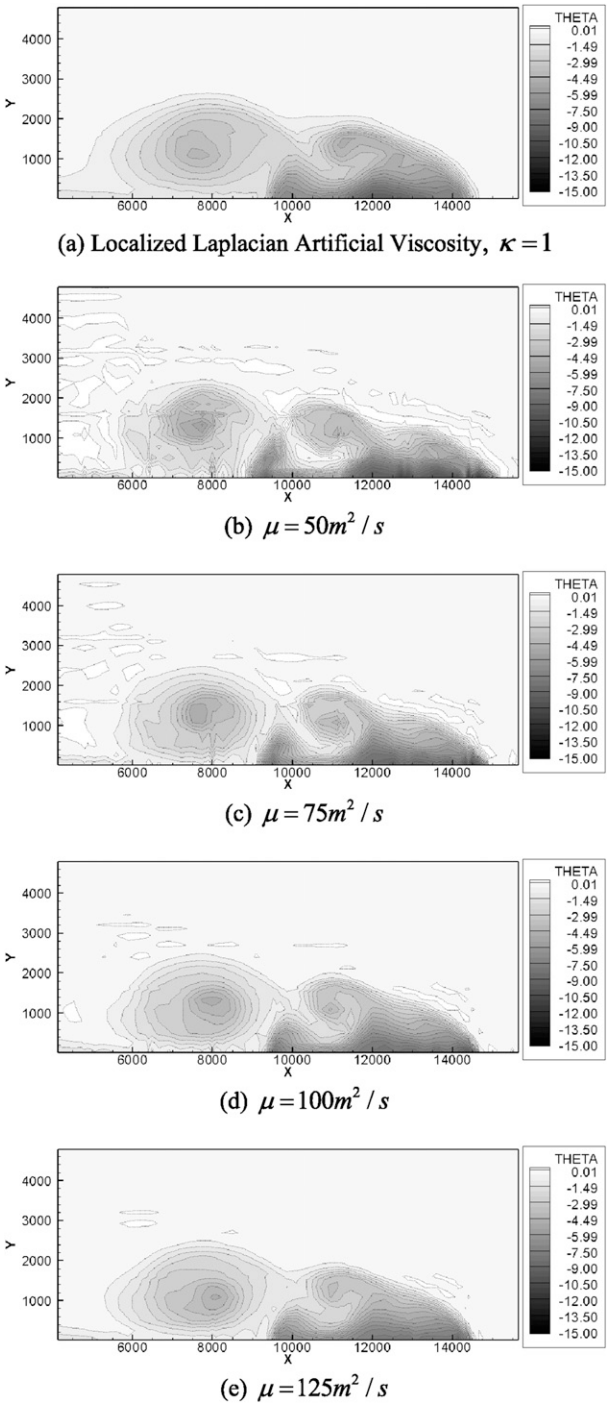

FIG. 17. Potential temperature perturbation fields of the rising thermal bubble flow at $t = 700$ s for localized artificial viscosity and constant viscosity with different μ using P^8 reconstruction on the 16×4 mesh. A total of 31 contour levels from -15.00 to 0.01 are used in the figure with every third contour level presented in the legend to avoid it being overly crowded.

TABLE 4. The maximum and minimum potential temperature perturbations $\theta'_{\max}$ and $\theta'_{\min}$ of the density current at $t = 900$ s for localized Laplacian artificial viscosity and constant viscosity with different μ using P^8 reconstruction on a 16×4 mesh.

	Max θ'	Min θ'
Localized Laplacian artificial viscosity	4.753×10^{-4}	-9.548
Constant viscosity, $\mu = 25\,\mathrm{m^2\,s^{-1}}$	Diverged	Diverged
Constant viscosity, $\mu = 50\,\mathrm{m^2\,s^{-1}}$	8.161×10^{-1}	-12.39
Constant viscosity, $\mu = 75\,\mathrm{m^2\,s^{-1}}$	1.981×10^{-1}	-10.85
Constant viscosity, $\mu = 100\,\mathrm{m^2\,s^{-1}}$	1.369×10^{-1}	-9.387
Constant viscosity, $\mu = 125\,\mathrm{m^2\,s^{-1}}$	9.243×10^{-2}	-8.835

viscosity method, $\mu = 2\,\mathrm{m^2\,s^{-1}}$ is considered to be a "large" viscosity value in the rising thermal bubble case, whereas $\mu = 25\,\mathrm{m^2\,s^{-1}}$ is considered to be a "small" viscosity value in the density current case. In contrast, the value of localized Laplacian artificial viscosity is automatically determined from both flow smoothness and numerical resolution features, with no parameter adjustment needed in simulations of different problems. To quantitatively judge the effect of the localized Laplacian artificial viscosity on nonhydrostatic mesoscale atmospheric modeling, we intentionally vary κ, a parameter in the artificial viscosity model distinguishing the nonsmooth range of the flow field, for the two benchmark atmospheric flow tests. It is observed in both cases that the small flow features near the thermal front are gradually damped as κ becomes larger.

It is concluded from all the simulation results that the proposed flow-feature-based localized Laplacian artificial viscosity method can sharply detect the nonsmooth flow features, and stabilize the DG discretization nearby. Furthermore, compared with the constant viscosity approach, the localized Laplacian artificial viscosity method works robustly for a wide range of grid sizes and polynomial orders without parameter tuning in the artificial viscosity model.

We will continue our work on the application of the developed localized Laplacian artificial viscosity and its extension to hyperviscosity for nonhydrostatic mesoscale atmospheric modeling. One example is the atmospheric flow over topography. In this case, when constant viscosity or hyperviscosity is used, mass and potential temperature can be diffused along terrain-following surfaces leading to a loss of hydrostatic balance and the generation of spurious vertical noise. The localized Laplacian artificial viscosity will be used to suppress disturbances in hydrostatic balance near topography by not triggering diffusion in smoothly varying fields over topography. Furthermore, we will also work on the following question: how to quantify the

interference between artificial viscosity and physically motivated diffusion in complex flow phenomena in which flow discontinuity or sharp fronts can interact with turbulence? It is likely that the interference between artificial viscosity and physically motivated diffusion can be minimized by using very high-order numerical schemes, which have sufficiently high resolution of smooth flow features, equipped with the localized Laplacian artificial viscosity stabilization technique. More results and discussion will be presented in future publications.

Acknowledgments. The authors are thankful to the anonymous reviewers for giving many excellent suggestions for improving this paper. Yu and Wang gratefully acknowledge the support of the Office of Naval Research through Award N000173-12-G902. The second author (FXG) gratefully acknowledges the support of the Office of Naval Research through Program Element PE-0602435N and the National Science Foundation (Division of Mathematical Sciences) through Program Element 121670.

REFERENCES

Atkins, H. L., and C.-W. Shu, 1998: Quadrature-free implementation of discontinuous Galerkin method for hyperbolic equations. *AIAA J.*, **36**, 775–782, doi:10.2514/2.436.

Barter, G. E., and D. L. Darmofal, 2010: Shock capturing with PDE-based artificial viscosity for DGFEM: Part I. Formulation. *J. Comput. Phys.*, **229**, 1810–1827, doi:10.1016/j.jcp.2009.11.010.

Bassi, F., and S. Rebay, 1994: Accurate 2D Euler computations by means of a high order discontinuous finite element method. *XIVth International Conference on Numerical Methods in Fluid Dynamics*, S. M. Deshpande, S. S. Desai, and R. Narasimha, Eds., Lecture Notes in Physics, Vol. 453, Springer, 234–240.

——, ——, G. Mariotti, S. Pedinotti, and M. Savini, 1997: A high-order accurate discontinuous finite element method for inviscid and viscous turbomachinery flows. *Second European Conference on Turbomachinery Fluid Dynamics and Thermodynamics*, R. Decuypere and G. Dibelius, Ed., Technologisch Instituut, 99–108.

Boyd, J. P., 1996: The Erfc-Log filter and the asymptotics of the Euler and Vandeven and sequence accelerations. *ICOSAHOM'95: Proc. Third Int. Conf. on Spectral and High Order Methods*, Houston, TX, University of Houston, 267–275.

Caramana, E. J., M. J. Shashkov, and P. P. Whalen, 1998: Formulations of artificial viscosity for multi-dimensional shock wave computations. *J. Comput. Phys.*, **144**, 70–97, doi:10.1006/jcph.1998.5989.

Cockburn, B., and C.-W. Shu, 1998: The Runge–Kutta discontinuous Galerkin finite element method for conservation laws V: Multidimensional systems. *J. Comput. Phys.*, **141**, 199–224, doi:10.1006/jcph.1998.5892.

Cook, A. W., 2007: Artificial fluid properties for large-eddy simulation of compressible turbulent mixing. *Phys. Fluids.*, **19**, 055103, doi:10.1063/1.2728937.

——, and W. H. Cabot, 2004: A high-wavenumber viscosity for high-resolution numerical methods. *J. Comput. Phys.*, **195**, 594–601, doi:10.1016/j.jcp.2003.10.012.

Dedner, A., and R. Klöfkorn, 2011: A generic stabilization approach for higher order discontinuous Galerkin methods for convection dominated problems. *J. Sci. Comput.*, **47**, 365–388, doi:10.1007/s10915-010-9448-0.

Giraldo, F. X., and M. Restelli, 2008: A study of spectral element and discontinuous Galerkin methods for the Navier-Stokes equations in nonhydrostatic mesoscale atmospheric modeling: Equations sets and test cases. *J. Comput. Phys.*, **227**, 3849–3877, doi:10.1016/j.jcp.2007.12.009.

——, J. F. Kelly, and E. M. Constantinescu, 2013: Implicit-explicit formulations for a 3D nonhydrostatic unified model of the atmosphere (NUMA). *SIAM J. Sci. Comput.*, **35**, B1162–B1194, doi:10.1137/120876034.

Guba, O., M. A. Taylor, P. A. Ullrich, J. R. Overfelt, and M. N. Levy, 2014: The spectral element method (SEM) on variable-resolution grids: Evaluating grid sensitivity and resolution-aware numerical viscosity. *Geosci. Model Dev.*, **7**, 2803–2816, doi:10.5194/gmd-7-2803-2014.

Guermond, J.-L., and R. Pasquetti, 2008: Entropy-based nonlinear viscosity for Fourier approximations of conservation laws. *C. R. Acad. Sci. Paris, Ser. I*, **346**, 801–806, doi:10.1016/j.crma.2008.05.013.

——, ——, and B. Popov, 2011: Entropy viscosity method for nonlinear conservation laws. *J. Comput. Phys.*, **230**, 4248–4267, doi:10.1016/j.jcp.2010.11.043.

Haga, T., and S. Kawai, 2013: Toward accurate simulation of shockwave-turbulence interaction on unstructured meshes: A coupling of high-order FR and LAD schemes. *21st AIAA Computational Fluid Dynamics Conf.*, San Diego, CA, AIAA, AIAA-2013-3065, doi:10.2514/6.2013-3065.

Harten, A., B. Engquist, S. Osher, and S. Chakravarthy, 1987: Uniformly high order essentially non-oscillatory schemes III. *J. Comput. Phys.*, **71**, 231–303, doi:10.1016/0021-9991(87)90031-3.

Hartmann, R., 2006: Adaptive discontinuous Galerkin methods with shock-capturing for the compressible Navier-Stokes equations. *Int. J. Numer. Methods Fluids*, **51**, 1131–1156, doi:10.1002/fld.1134.

——, and P. Houston, 2002: Adaptive discontinuous Galerkin finite element methods for the compressible Euler equations. *J. Comput. Phys.*, **183**, 508–532, doi:10.1006/jcph.2002.7206.

Hesthaven, J. S., and T. Warburton, 2008: *Nodal Discontinuous Galerkin Methods: Algorithms, Analysis, and Applications.* Springer-Verlag, 502 pp.

Huang, P. G., Z. J. Wang, and Y. Liu, 2005: An implicit space-time spectral difference method for discontinuity capturing using adaptive polynomials. *17th AIAA Computational Fluid Dynamics Conf.*, Toronto, ON, Canada, AIAA, AIAA-2005-5255, doi:10.2514/6.2005-5255.

Hughes, T., and M. Mallet, 1986: A new finite element formulation for computational fluid dynamics. IV. A discontinuity-capturing operator for multidimensional advective-diffusive systems. *Comput. Methods Appl. Mech. Eng.*, **58**, 329–336, doi:10.1016/0045-7825(86)90153-2.

Jameson, A., 1995: Analysis and design of numerical schemes for gas dynamics, 2: Artificial diffusion and discrete shock structure. *Int. J. Comput. Fluid Dyn.*, **5**, 1–38, doi:10.1080/10618569508940734.

Jebens, S., O. Knoth, and R. Weiner, 2009: Explicit two-step peer methods for the compressible Euler equations. *Mon. Wea. Rev.*, **137**, 2380–2392, doi:10.1175/2008MWR2671.1.

Jiang, G. S., and C.-W. Shu, 1996: Efficient implementation of weighted ENO schemes. *J. Comput. Phys.*, **126**, 202–228, doi:10.1006/jcph.1996.0130.

Johnson, C., A. Szepessy, and P. Hansbo, 1990: On the convergence of shock-capturing streamline diffusion finite element methods for hyperbolic conservation laws. *Math. Comput.*, **54**, 107–129, doi:10.1090/S0025-5718-1990-0995210-0.

Kawai, S., and S. Lele, 2008: Localized artificial diffusivity scheme for discontinuity capturing on curvilinear meshes. *J. Comput. Phys.*, **227**, 9498–9526, doi:10.1016/j.jcp.2008.06.034.

——, S. K. Shankar, and S. K. Lele, 2010: Assessment of localized artificial diffusivity scheme for large-eddy simulation of compressible turbulent flows. *J. Comput. Phys.*, **229**, 1739–1762, doi:10.1016/j.jcp.2009.11.005.

Kelly, J. F., and F. X. Giraldo, 2012: Continuous and discontinuous Galerkin methods for a scalable 3D nonhydrostatic atmospheric model: Limited-area mode. *J. Comput. Phys.*, **231**, 7988–8008, doi:10.1016/j.jcp.2012.04.042.

Klemp, J. B., W. C. Skamarock, and J. Dudhia, 2007: Conservative split-explicit time integration methods for the compressible nonhydrostatic equations. *Mon. Wea. Rev.*, **135**, 2897–2913, doi:10.1175/MWR3440.1.

Klöckner, A., T. Warburton, and J. S. Hesthaven, 2011: Viscous shock capturing in a time-explicit discontinuous Galerkin method. *Math. Model. Nat. Phenom.*, **6**, 57–83, doi:10.1051/mmnp/20116303.

Kolev, T. V., and R. N. Rieben, 2009: A tensor artificial viscosity using a finite element approach. *J. Comput. Phys.*, **228**, 8336–8366, doi:10.1016/j.jcp.2009.08.010.

Kopera, M. A., and F. X. Giraldo, 2014: Analysis of adaptive mesh refinement for IMEX discontinuous Galerkin solutions of the compressible Euler equations with application to atmospheric simulations. *J. Comput. Phys.*, **275**, 92–117, doi:10.1016/j.jcp.2014.06.026.

Kurganov, A., and Y. Liu, 2012: New adaptive artificial viscosity method for hyperbolic systems of conservation laws. *J. Comput. Phys.*, **231**, 8114–8132, doi:10.1016/j.jcp.2012.07.040.

Li, X. L., C. G. Chen, X. S. Shen, and F. Xiao, 2013: A multimoment constrained finite-volume model for nonhydrostatic atmospheric dynamics. *Mon. Wea. Rev.*, **141**, 1216–1240, doi:10.1175/MWR-D-12-00144.1.

Lynch, P., 2008: The origins of computer weather prediction and climate modeling. *J. Comput. Phys.*, **227**, 3431–3444, doi:10.1016/j.jcp.2007.02.034.

Marras, S., J. F. Kelly, F. X. Giraldo, and M. Vazquez, 2012: Variational multiscale stabilization of high-order spectral elements for the advection-diffusion equation. *J. Comput. Phys.*, **231**, 7187–7213, doi:10.1016/j.jcp.2012.06.028.

——, M. Moragues, M. Vazquez, O. Jorba, and G. Houzeaux, 2013: A variational multiscale stabilization finite element method for the solution of the Euler equations of non hydrostatic stratified flows. *J. Comput. Phys.*, **236**, 380–407, doi:10.1016/j.jcp.2012.10.056.

——, and Coauthors, 2015: A review of element-based Galerkin methods for numerical weather prediction: Finite elements, spectral elements, and discontinuous Galerkin. *Arch. Comput. Methods Eng.*, doi:10.1007/s11831-015-9152-1, in press.

Nair, R. D., 2009: Diffusion experiments with a global discontinuous Galerkin shallow-water model. *Mon. Wea. Rev.*, **137**, 3339–3350, doi:10.1175/2009MWR2843.1.

Oberai, A. A., and J. Wanderer, 2006: A dynamic multiscale viscosity method for the spectral approximation of conservation laws. *Comput. Methods Appl. Mech. Eng.*, **195**, 1778–1792, doi:10.1016/j.cma.2005.05.035.

Olson, B. J., and S. K. Lele, 2013: Directional artificial fluid properties for compressible large-eddy simulation. *J. Comput. Phys.*, **246**, 207–220, doi:10.1016/j.jcp.2013.03.026.

Park, J. S., M. L. Yu, C. Kim, and Z. J. Wang, 2014: Comparative study of shock-capturing methods for high-order CPR: MLP and artificial viscosity. *Eighth Int. Conf. on Computational Fluid Dynamics*, Chengdu, China, ICCFD, ICCFD8-2014-0067.

Persson, P.-O., 2013: Shock capturing for high-order discontinuous Galerkin simulation of transient flow problems. *Proc. 21st AIAA Computational Fluid Dynamics Conf.*, San Diego, CA, AIAA, AIAA-2013-3061. [Available online at http://persson.berkeley.edu/pub/persson13transient_shocks.pdf.]

——, and J. Peraire, 2006: Sub-cell shock capturing for discontinuous Galerkin methods. *Proc. 44th AIAA Aerospace Sciences Meeting and Exhibit*, Reno, NV, AIAA, AIAA-2006-112.

Premasuthan, S., C. Liang, and A. Jameson, 2010: Computation of flows with shocks using spectral difference scheme with artificial viscosity. *Proc. 48th AIAA Aerospace Sciences Meeting Including the New Horizons Forum and Aerospace Exposition*, Orlando, FL, AIAA, AIAA-2010-1449.

Qiu, J. X., and C.-W. Shu, 2005: Runge–Kutta discontinuous Galerkin method using WENO limiters. *SIAM J. Sci. Comput.*, **26**, 907–929, doi:10.1137/S1064827503425298.

Reisner, J., J. Serencsa, and S. Shkoller, 2013: A space–time smooth artificial viscosity method for nonlinear conservation laws. *J. Comput. Phys.*, **235**, 912–933, doi:10.1016/j.jcp.2012.08.027.

Schär, C., D. Leuenberger, O. Fuhrer, D. Lüthi, and C. Girard, 2002: A new terrain-following vertical coordinate formulation for atmospheric prediction models. *Mon. Wea. Rev.*, **130**, 2459–2480, doi:10.1175/1520-0493(2002)130<2459:ANTFVC>2.0.CO;2.

Shu, C.-W., and S. Osher, 1989: Efficient implementation of essentially non-oscillatory shock-capturing schemes. II. *J. Comput. Phys.*, **83**, 32–78, doi:10.1016/0021-9991(89)90222-2.

Skamarock, W. C., and J. B. Klemp, 2008: A time-split nonhydrostatic atmospheric model for weather research and forecasting applications. *J. Comput. Phys.*, **227**, 3465–3485, doi:10.1016/j.jcp.2007.01.037.

Steppeler, J., R. Hess, U. Schättler, and L. Bonaventura, 2003: Review of numerical methods for nonhydrostatic weather prediction models. *Meteor. Atmos. Phys.*, **82**, 287–301, doi:10.1007/s00703-001-0593-8.

Tadmor, E., 1990: Shock capturing by the spectral viscosity method. *Comput. Methods Appl. Mech. Eng.*, **80**, 197–208, doi:10.1016/0045-7825(90)90023-F.

Tezduyar, T. E., and Y. J. Park, 1986: Discontinuity-capturing finite element formulations for nonlinear convection-diffusion-reaction equations. *Comput. Methods Appl. Mech. Eng.*, **59**, 307–325, doi:10.1016/0045-7825(86)90003-4.

——, and M. Senga, 2006: Stabilization and shock-capturing parameters in SUPG formulation of compressible flows. *Comput. Methods Appl. Mech. Eng.*, **195**, 1621–1632, doi:10.1016/j.cma.2005.05.032.

Ullrich, P. A., and C. Jablonowski, 2012: MCore: A nonhydrostatic atmospheric dynamical core utilizing high-order finite-volume methods. *J. Comput. Phys.*, **231**, 5078–5108, doi:10.1016/j.jcp.2012.04.024.

Von Neumann, J., and R. D. Richtmyer, 1950: A method for the numerical calculation of hydrodynamic shocks. *J. Appl. Phys.*, **21**, 232–237, doi:10.1063/1.1699639.

Wicker, L. J., and W. C. Skamarock, 1998: A time-splitting scheme for the elastic equations incorporating second-order Runge–Kutta time differencing. *Mon. Wea. Rev.*, **126**, 1992–1999, doi:10.1175/1520-0493(1998)126<1992:ATSSFT>2.0.CO;2.

Xue, M., 2000: High-order monotonic numerical diffusion and smoothing. *Mon. Wea. Rev.*, **128**, 2853–2864, doi:10.1175/1520-0493(2000)128<2853:HOMNDA>2.0.CO;2.

Yang, M., and Z. Wang, 2009: A parameter-free generalized moment limiter for high-order methods on unstructured grids. *Adv. Appl. Math. Mech.*, **1**, 451–480, doi:10.4208/aamm.09-m0913.

Yelash, L., A. Mueller, M. Lukacova-Medvidova, F. X. Giraldo, and V. Wirth, 2014: Adaptive discontinuous evolution Galerkin method for dry atmospheric flow. *J. Comput. Phys.*, **268**, 106–133, doi:10.1016/j.jcp.2014.02.034.

Yu, M. L., and Z. J. Wang, 2014: Shock capturing for the correction procedure via reconstruction method using artificial viscosity and diffusivity. *Proc. Eighth ICCFD Conf.*, Chengdu, China, ICCFD, ICCFD8-2014-0079.

——, ——, and Y. Liu, 2014: On the accuracy and efficiency of discontinuous Galerkin, spectral difference and correction procedure via reconstruction methods. *J. Comput. Phys.*, **259**, 70–95, doi:10.1016/j.jcp.2013.11.023.

Zhang, X., and C.-W. Shu, 2010: On positivity preserving high order discontinuous Galerkin schemes for compressible Euler equations on rectangular meshes. *J. Comput. Phys.*, **229**, 8918–8934, doi:10.1016/j.jcp.2010.08.016.

Zhang, Y. F., and R. D. Nair, 2012: A nonoscillatory discontinuous Galerkin transport scheme on the cubed sphere. *Mon. Wea. Rev.*, **140**, 3106–3126, doi:10.1175/MWR-D-11-00287.1.

Zingan, V., J.-L. Guermond, J. Morel, and B. Popov, 2013: Implementation of the entropy viscosity method with the discontinuous Galerkin method. *Comput. Methods Appl. Mech. Eng.*, **253**, 479–490, doi:10.1016/j.cma.2012.08.018.